Nicolaus Copernicus University
Faculty of Physics, Astronomy and Informatics
Institute of Physics

Robiatul Adawia
Index number: 315473

Master thesis
in the field of Physics

Studies of Stability of Nagaoka Ferromagnetism on a Triangular Lattice

Supervisor
dr hab. inż. Paweł Potasz
Institute of Physics, NCU

Toruń, September 2024

I acknowledge and accept this thesis

.....
date and supervisor's signature

I confirm submitting a thesis

.....
date and signature of Dean's Office

Abstract

Moiré superlattices can be created by stacking two atomic layers of different materials, and its electronic properties can be manipulated using easily adjustable external factors, such as the twist angle, making them promising candidates for quantum simulators. In this study, first we briefly examine the features of the triangular moire lattice of transition metal dichalcogenides (TMDs) by treating it as a periodic system through both continuum and tight-binding models. The primary aim is to investigate the magnetic characteristics by fully incorporating correlations, which is challenging in a periodic system due to the vast size of the Hilbert space. Therefore, we concentrate on finite-sized triangular lattices.

We examine the finite-size twisted TMDs within a moiré triangular lattice and analyze their magnetic properties above half-filling. By introducing one electron into a half-filled system, the total spin of the ground state can reach its maximum, leading to the emergence of Nagaoka ferromagnetism. This form of magnetism arises from correlation effects, essentially due to constructive interference among various many-body configurations. We employ exact diagonalization methods to solve the Hubbard Hamiltonian, fully accounting for these correlations. We demonstrate the emergence of Nagaoka ferromagnetism by adding one, two, and three electrons above half-filling, with the ferromagnetic characteristics varying based on the geometries of finite triangular lattices. Additionally, the interaction strength is analyzed to observe transitions in total spin and assess system stability. The Nagaoka polaron is also visualized within the finite triangular lattices.

Declaration

I, Robiatul Adawia, hereby declare that this thesis entitled "Studies of Stability of Nagaoka Ferromagnetism on a Triangular Lattice" is entirely my own work, based on research conducted by me, under the supervision of Dr. hab. Paweł Potasz at Uniwersytet Mikolaja Kopernika. All sources used or referred to have been properly acknowledged in the bibliography. I affirm that:

1. This thesis is original, and all ideas, analyses, interpretations, and conclusions presented herein are my own, except where explicitly stated otherwise.
2. The research presented in this thesis has not been submitted for any other degree or qualification at any other university or institution.
3. Any assistance received in the preparation of this thesis, including technical and editorial support, has been duly acknowledged.
4. Any data or materials obtained from external sources have been appropriately cited and referenced.
5. The research conducted and presented in this thesis adheres to ethical guidelines and standards applicable to the field of study.

I understand that any breach of academic integrity or ethical conduct may result in disciplinary action, including the revocation of my degree.

Robiatul Adawia

Contents

List of Figures

1 Introduction

This section provides a brief overview of the moiré superlattice and its unique characteristics, and using the hubbard model as a method to do simulation. From the simulation we may observe the magnetic characteristic of the system that arises when particles like electrons on the lattice are above half-filling, which is known as Nagaoka ferromagnetism.

1.1 Moiré Superlattice

Moiré patterns, by definition, occur when two periodic patterns are superimposed with a slight rotation (see Figure 1). In solid states, moiré patterns or moiré structures on layered materials have been observed and it can be generated through rotation between layers or mechanical disruption of the crystal structure [8]. Initially, this pattern did not receive much attention, until the advent of graphene then it was realized that moiré structures were an effective way of tuning band structure [1]. By modifying the moiré structure, it can influence the energy levels distribution, which can affect the material's electrical, optical, and magnetic properties.

The moiré structure "lattice" or repeating pattern is larger (expanding to several nanometers) compared to the conventional materials structure which is in an atomic scale. This larger size makes it easier to study in the experiment using optical and other measurement techniques. Additionally, since it is two-dimensional (2D) we can examine the entire surface using techniques that focus on surface observation such as scanning tunneling microscopy (STM) [8–10].

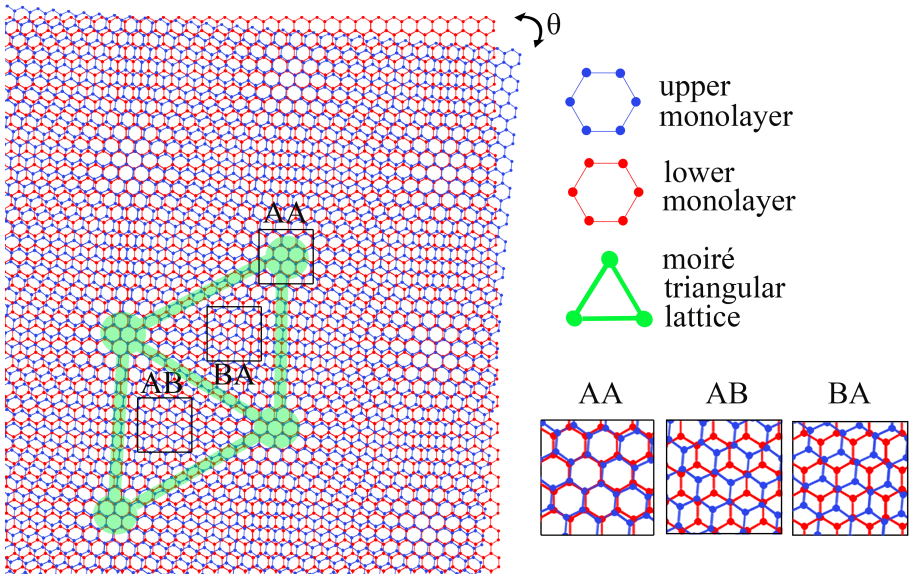

Fig. 1: Illustration of two atomic layers with hexagonal unit cells, twisted with angle θ, forming triangular moiré structure (green shape). The AA stacking is aligned configuration and AB (BA) stacking is misaligned configuration [1].

The 2D layered materials that were mentioned before are known as van der Waals (vdW) materials such as hexagonal boron nitride (hBN), graphene, and

transition metal dichalcogenides (TMDs) [11]. These materials consist of one or several atomic layers bonded strongly by covalent or ionic interactions within the layers, while vdW forces are sufficient to stack them between layers. VdW heterostructures can be formed by stacking different structures using "tear and stack" technique [12] without requiring lattice matching. By carefully selecting and stacking different materials, one can engineer band structures, control charge carrier mobility, and introduce new physical phenomena like tunneling and charge transfer.

The distinctive feature of a moiré superlattice is the appearance of flat bands especially at certain 'magic angle' (e.g. 1.1°) which first observed in twisted bilayer graphene (TGB) [10,13]. These flat bands occur when the band structure flattens close to zero Fermi energy due to strong coupling between layers. The flat low-energy bands are expected to have wave functions that are localized in real space, which are notably concentrated in AA stacking areas (where the layers are aligned, as shown in Figure 1). AA has a high local density of states while in contrast, the wave functions in region AB (BA) stacking exhibit very low density states.

Localization of the wave function implies that electrons have limited freedom to move throughout the lattice, with minimal overlap between different regions (such as AA and AB). As a result, the energy levels of electrons don't change much with momentum which leads to weak dispersion. This weak dispersion in momentum space means the kinetic energy is substantially lower than the on-site Coulomb interaction [13].

The interaction between electron-electrons will form strong correlation phases, where they behave in a highly interdependent manner and generate complex properties. Several phases related to interparticle interactions have been already observed, like Mott insulator states at one hole per moiré superlattice unit cell or generalized Wigner crystal states at other partial fillings [14–16]. Additionally, high density states of flat bands can give rise to exotic quantum phenomena such as superconductivity and unconventional superconductivity [17].

1.2 Transition Metal Dichalcogenides (TMDs)

The maxima and minima of local density states of moiré lattice are arranged periodically forming triangular, rectangular, hexagonal or other arrangement depending on the materials [8]. Our focus is on twisted structures forming triangular lattices as in Figure 1. TBG is one example of twisted material that forms triangular lattices, but our main interest is in transition metal dichalcogenides (TMDs) which have electronic bandgap [2].

TMDs are composed of transition-metal elements from groups IV-X of the periodic table (e.g., Mo, W) combined with chalcogen elements (e.g., S, Se, Te) [2, 18]. The typical structure of monolayer TMDs resembles a sandwich, with one layer of metal atoms placed between two layers of chalcogen atoms

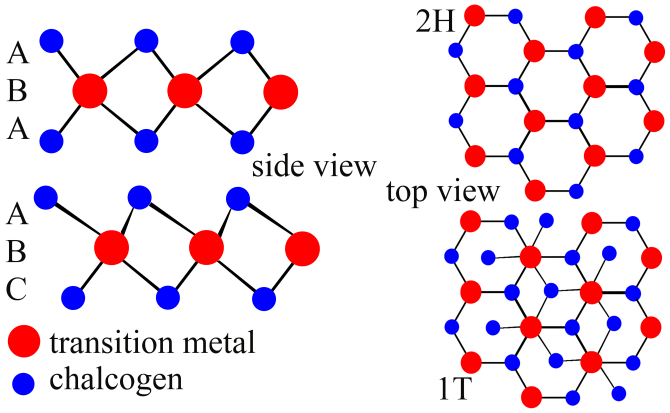

Fig. 2: In TMD monolayers, the ABA stacking configuration features aligned chalcogens and is referred to as the 2H phase, whereas the ABC stacking configuration is with mismatched chalcogens (1T phase) [2,3].

(technically, it consists of 3 atomic layers, see Fig.2). Some examples of TMDs are molybdenum disulfide (MoS_2), tungsten disulfide (WS_2), molybdenum diselenide ($MoSe_2$), and tungsten diselenide (WSe_2).

1.2.1 TMDs electronic properties

Experimental studies have revealed that the band structure of TMDs transitions from an indirect energy gap (bandgap) to a direct bandgap when its bulk structure is reduced to a monolayer [19–21] due to the lack of interaction between layers. Light emission is much more efficient in direct bandgap and simpler in the engineering of electronic devices. In addition, TMDs bandgap is tunable and can be regulated by external factors like the twist angle, making them good candidates for quantum simulators [18].

Two important characteristics of TMD monolayer are inversion symmetry and strong spin-orbit coupling (SOC) [2, 3, 21]. Inversion symmetry occurs when the physical properties of a structure remain the same after inverting its spatial configuration, as it is in bulk MoS_2. In monolayer, the inversion symmetry is broken due to asymmetrical arrangement between chalcogen atoms.

SOC is the relativistic effect of interaction between an electron's spin and its orbital motion around the nucleus causing splitting in the electron energy levels depending on their spin orientation (see Figure 3). In structures that have inversion symmetry the SOC effects cancel out because the spin-orbit is symmetrically distributed. The SOC effects persist and become more pronounced when the symmetry is broken, and the coupling is especially strong in TMDs monolayer as the atomic number of the transition metal atoms rises [21].

The interplay of these properties leads to controllable spin-valley coupling, meaning that valley polarization of charge carriers directly influences spin polarization [2]. Spin-valley coupling in TMDs occurs in band edge K-K' valleys within the Brillouin zone (Fig.3), meaning that electrons in the K valley have an opposite spin orientation to those in the K' valley as a consequence of time-reversal symmetry [3]. In monolayer, the K-K' valleys are the key areas where

the conduction band minimum and valence band maximum are located. This inherent characteristic could be utilized to develop spintronic devices without the need for magnetic materials.

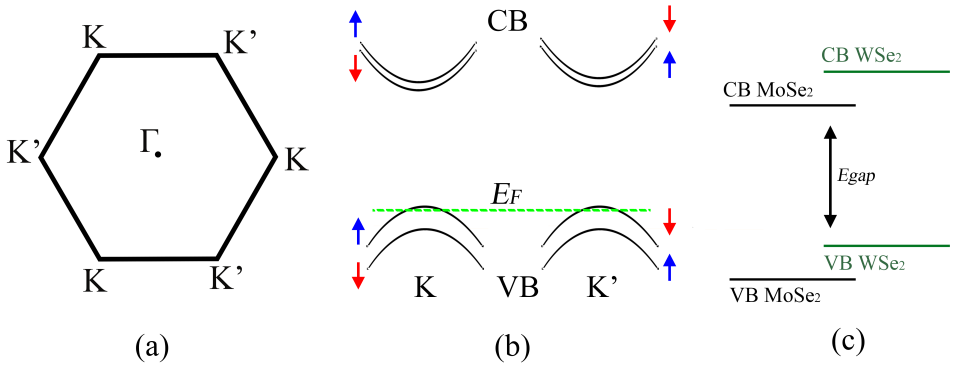

Fig. 3: (a) K-K' valleys in the Brillouin zone [3]; (b) Valley splitting leads to spin splitting, the splitting in highest valence band (VB) larger than in conduction band (CB) [4]; (c) In a direct bandgap $MoSe_2/WSe_2$ heterostructure, the VB and CB originate from different layers [5].

1.2.2 Triangular moiré lattice of TMDs

The formation of a triangular moiré lattice in TMDs can be achieved either by twisting monolayers at small angles or it emerges due to mismatch of stacked heterostructures with different lattice constants [5, 18]. In twisted bilayer configuration, AA stacking (see Fig.1) occurs when the transition metal atoms align directly with each other (denoted as MM), while AB (or BA) stacking refers to a mismatch between the metal and chalcogen atoms (MX or XM). In MM stacking the overlap of the wavefunctions from both layers is considerable, resulting in a strong interaction or strong coupling, whereas the coupling in the XM (MX) is weaker [22]. Examples of TMD heterostructures include $MoSe_2/WSe_2$, WSe_2/MoS_2, and WSe_2/WS_2.

The direct band gap persists even though the edges of the valence and conduction bands, which remain within the K valleys, are situated in different layers [5,22]. This happens due to strong coupling, where the overlapping wave functions between the layers create hybridized states with electronic properties distinct from those of the individual layers. Figure 3 shows the narrow band gap formed between the conduction band minima of $MoSe_2$ and the valence band maxima of WSe_2.

In twisted TMDs, the emergence of flat bands can drive the system into a Mott insulating state [4, 15, 23]. When the system is at half-filling (number of electrons equal to number of moire lattice), the flat bands amplify electron-electron interactions and strong repulsion between electrons leads to their localization yielding insulating behavior. One way to regulate this insulating state is by adjusting the twist angles.

1.3 Theoretical methods: continuum, tight-binding, and Hubbard model

In a crystal lattice system, the distance between charge carriers (electrons or holes) corresponds to the atomic spacing [18]. In contrast, a single charge carrier in the moiré superlattice is affected by thousands of atoms which act as a long-period potential (moiré potential). The formation of the moiré lattice alters the electronic energy bands, resulting in moiré bands. For instance, in WSe_2/WS_2, the valence moiré bands are formed by holes in WSe_2 moving within the periodic moiré potential. As a result, TMD superlattices offer a solid platform for exploring many-body physics.

Here we give a short explanation of the methods that are used in this work for solving TMD moiré triangular lattice systems, i.e. continuum model, tight-binding, and hubbard model. The three methods are commonly used for the system of particles in crystal lattices. For more detail explanations are provided in Chapter 2 Methodology.

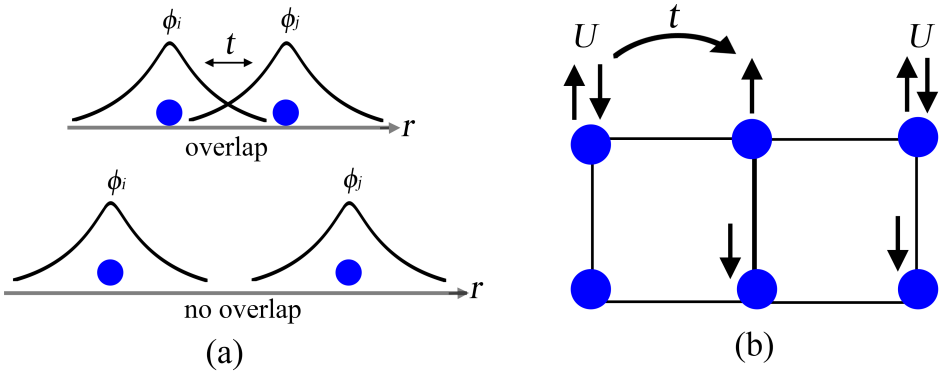

Fig. 4: (a) The proximity of overlapping orbital wave functions ϕ causes electrons to jump to nearest neighbor orbitals with hopping energy t [6]. (b) When two electrons occupy the same orbital with different spin ($\uparrow$ and $\downarrow$), the energy to resist electron repulsion is the on-site Coulomb energy U [ref???]

Continuum model. This model is within a single-particle picture where the behavior of particles is described individually without considering interaction between particles. The low-energy of moiré band can be calculated using the continuum effective Hamiltonian model as the system is periodic [1,4]. Bloch's theorem is applicable at any twist angle due to hopping in this model is both local and periodic. The electron hopping between layers is localized, meaning that the interaction is determined by the specific position within the lattice. In areas with MM stacking, the coupling is stronger, making it easier for hopping to occur in those regions. Following the principles of Bloch's theorem, the numerical solution for moiré energies is solved using plane wave expansion.

Tight-binding model. This model is also within a single-particle picture and provides a more detailed approach by taking into account the atomic structure. Electrons are tightly bound to the atomic orbital and it can move or hop to neighboring sites due to the overlap of their nuclei wave functions [24]. In

a moiré lattice, electrons can hop either within the same layer or between different layers. The tight-binding Hamiltonian model includes terms for both on-site energies U and hopping integrals t. By appropriate mapping, one can transit from a continuum model to a tight-binding model for a given energy band.

Hubbard model. John Hubbard proposed a model in 1963 to study the interactions of electrons in the narrow energy bands of transition metals [25]. This model introduces an on-site interaction term that accounts for the energy cost when two electrons occupy the same atomic site, in addition to the hopping term that describes electron movement between sites. Essentially, the Hubbard model is a more detailed version of the tight-binding model that incorporates electron-electron interactions. In moiré superlattices, this model can be used to investigate correlation effects.

The moiré band structure in TMD bilayers is much simpler [18], allowing the moiré system to be represented as a single band with two fold-degeneracy that comes from spin-orbit splitting. Observation is focusing on the valence band where a large spin splitting happens. Thus from these considerations we can use the single-band Hubbard model. In addition, heterobilayers are chosen to avoid degeneracy that comes from both layers.

1.4 Moiré magnetism

The emergence of magnetic properties due to exchange interaction has been observed in vdW materials which can be categorized based on their magnetic order, such as ferromagnetic or antiferromagnetic states [26–28]. In ferromagnetic exchange interaction, electron spins align in the same direction to minimize energy, whereas in antiferromagnetic exchange, spins align in opposite directions. The Pauli exclusion principle and on-site Coulomb interaction are key factors that influence the spin arrangement in these materials. In heterostructures, one layer can alter the magnetic properties of another, leading to magnetism that can be controlled or tuned.

Experimental study has shown that moiré patterns in twisted vdW materials can generate magnetic properties in the system [29]. This study investigates magnetic properties by slightly varying the twist angle. Moiré lattices are known for their significant correlation effects, so the interaction between moiré potential and exchange interactions between layers leads to the formation of new magnetic states.

1.4.1 Nagaoka ferromagnetism

In 1966 Nagaoka studied the emergence of ferromagnetic states, known as Nagaoka ferromagnetism [30], purely from electron-electron interaction due strongly correlated systems. The model is assumed to be half-filled states (the number of sites equal to the number of electrons) with one hole added to the system. Due to strong on-site repulsion, this hole itinerant and polarized the

spin of surrounding electrons. The analysis is based on the Hubbard model in a narrow conduction band with on-site Coulomb interaction much larger than the hopping integral.

Experimental studies on Nagaoka ferromagnetism have been performed on (2x2) quantum dots [31, 32] with configurations of three electrons in four sites (almost half-filling). As it is already shown by Nagaoka, a single hole in this setup induces a ferromagnetic ground state by facilitating constructive interference when the system has maximum total spin.

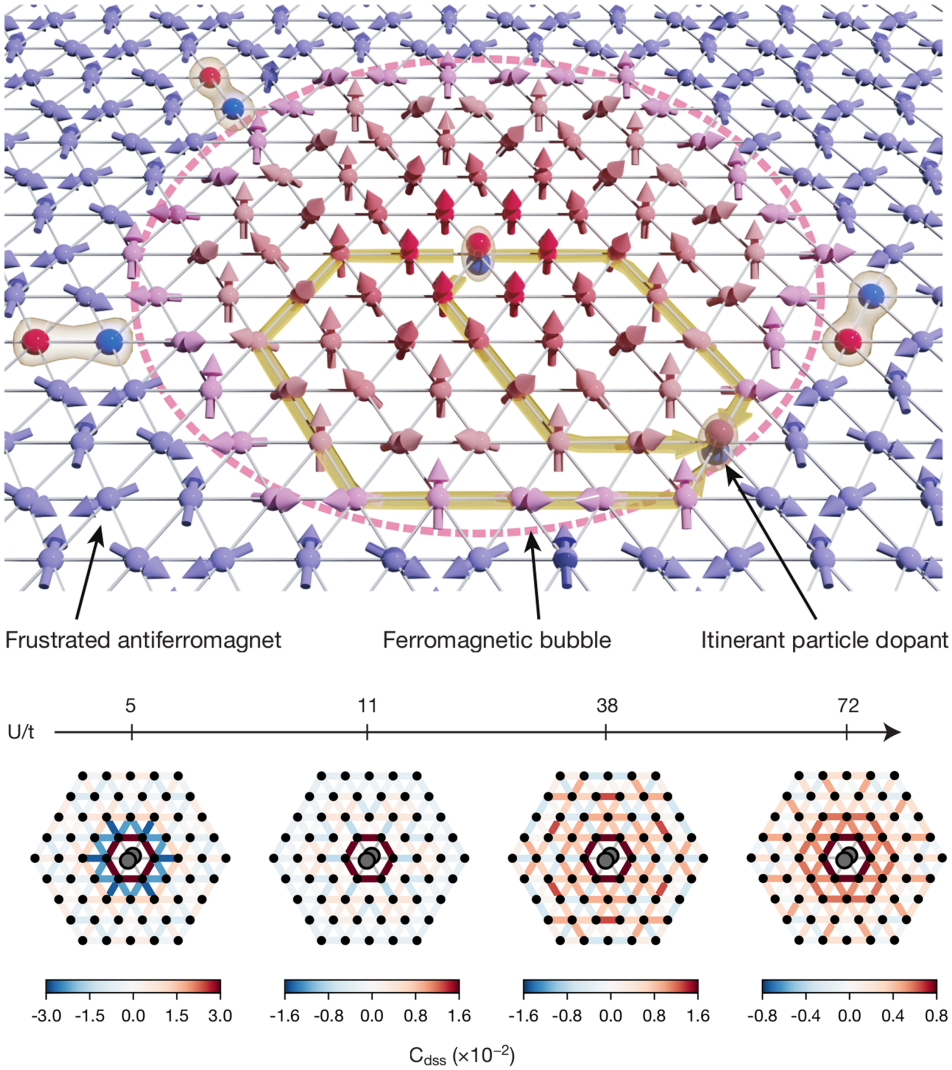

Fig. 5: (Above) An illustration from Ref. [7] demonstrating how introducing holes into a half-filled system can polarize the surrounding electron spins around the hole. (Below) The interaction strength ($\frac{U}{t}$) represents the ratio between the on-site Coulomb interaction U and the hopping integral t. A higher interaction strength results in a larger area influenced by the Nagaoka bubble.

Another experimental study was conducted on a larger system, involving the observation of ultracold fermions in a tunable triangular optical lattice [7]. Nagaoka polarons, a localized Nagaoka ferromagnet, were observed in the experiment (see Fig.5). These polarons formed as a result of doping a single hole

for each smaller region in a half-filled system, with the polaron's size reaching up to 30 sites. The experiment involves preparing the material with half-filled particles. Then, additional holes are introduced as dopants. These holes act as itinerant and polarize the surrounding region, with the extent of the affected area determined by the ratio between on-site interaction and hopping energy. A higher ratio leads to a larger region being polarized by each dopant electron.

2 Methodology

This section offers a thorough explanation of the mathematical model and the procedure for conducting this computational experiment. We examine the TMD moire triangular lattice with continuum model and with tight binding as a case study, and Hubbard model as our primary focus. We also provide a detailed explanation on solving the Hubbard system using Exact Diagonalization method.

2.1 Continuum model: single particle approximation

A continuum model describes crystal structure as a continuous matter that fills the occupied spaces, by neglecting that matter consists of discrete smallest components such as atoms. This method employs a single-particle approximation where the interaction of electrons and nuclei is described as an effective one-electron potential $U(\boldsymbol{r})$, and electron-electron interactions are neglected. This model is good for studying large systems such as bulk matter.

In a perfectly periodic lattice, the effective potential must fulfill the characteristic periodicity, meaning each lattice site has identical localized potentials [6],

$$U(\boldsymbol{r} + \boldsymbol{R}) = U(\boldsymbol{r}), \tag{1}$$

in two-dimensional (2D) cases, $\boldsymbol{r}$ is the lattice position vector and $\boldsymbol{R}$ is the Bravais lattice vector that have general form as,

$$\boldsymbol{R} = n_1\boldsymbol{a}_1 + n_2\boldsymbol{a}_2.$$

n_1, n_2 are integer numbers, $\boldsymbol{a_1}, \boldsymbol{a_2}$ are lattice vectors in real space with $\boldsymbol{a_i}$ can be expressed as $a_i(x, y)$ in Cartesian coordinates. To obtain the energy eigenvalues and eigenvectors of the system, it is necessary to solve the time-independent Schrödinger equation for a single particle with mass m:

$$\hat{H}|\psi(\boldsymbol{r})\rangle = E|\psi(\boldsymbol{r})\rangle, \tag{2}$$

where $|\psi(\boldsymbol{r})\rangle$ is a state function. The Hamiltonian operator $\hat{H}$ consists of kinetic energy and the effective potential

$$\hat{H} = -\frac{\hbar^2}{2m}\nabla^2 + U(\boldsymbol{r}), \tag{3}$$

with $\nabla^2 = \frac{\partial^2}{\partial x^2} + \frac{\partial^2}{\partial y^2}$. For simplicity, all operators will be written without a hat ($\hat{}$) from this point forward.

The solution for Eq.2 is derived from Bloch's theorem, which asserts that the wavefunctions of electrons in a periodic potential can be represented as a plane wave multiplied by a periodicity function

$$|\psi(\boldsymbol{r})\rangle = e^{i\boldsymbol{k}\cdot\boldsymbol{r}}u(\boldsymbol{r}), \tag{4}$$

known as the Bloch's wavefunction. $u(\boldsymbol{r}) = u(\boldsymbol{r} + \boldsymbol{R})$ is the Barvais lattice periodic function which obey Eq.1, thus we can show

$$|\psi(\boldsymbol{r} + \boldsymbol{R})\rangle = e^{i\boldsymbol{k}\cdot\boldsymbol{R}}|\psi(\boldsymbol{r})\rangle. \tag{5}$$

$\boldsymbol{k}$ represents wave vectors that characterize the momentum states of electrons. In reciprocal space (momentum space), $\boldsymbol{k}$ is defined as

$$\boldsymbol{k} = x_1\boldsymbol{b}_1 + x_2\boldsymbol{b}_2. \tag{6}$$

x_1, x_2 are real and $\boldsymbol{b}_1, \boldsymbol{b}_2$ are reciprocal lattice vectors (a reciprocal space basis, called G-basis, can be formed from linear combinations of $\boldsymbol{b}_{1,2}$ vectors, $\boldsymbol{G}_{i,j} = i\boldsymbol{b}_1 + j\boldsymbol{b}_2$, i, j-integers).

The periodic potential of lattices is defined in reciprocal space through Fourier transform, and $\boldsymbol{b}_j$ correspond to $\boldsymbol{a}_i$ by satisfying

$$\boldsymbol{a}_i \cdot \boldsymbol{b}_j = 2\pi\delta_{ij}, \tag{7}$$

δ_{ij} is Dirac delta. The electronic properties of a system, including energy bands, can be analyzed using a particular region in reciprocal space called the Brillouin zone. The behavior of wavefunctions within the Brillouin zone described by the wave vector $\boldsymbol{k}$, which indicates how the wavefunction is distributed in space.

2.1.1 Case: Continuum model for moiré triangular superlattice

In this section we apply the continuum model in TMDs moiré triangular superlattice. We start from constructing the 2D triangular lattice system in real space with [33, 34]:

$$\boldsymbol{a_1} = a_M\big(-\frac{1}{2},\ \frac{1}{2}\sqrt{3}\big), \tag{8a}$$

$$\boldsymbol{a_2} = a_M\big(\frac{1}{2},\ \frac{1}{2}\sqrt{3}\big), \tag{8b}$$

where a_M epresents the moiré period or lattice twist angle. The moiré period is obtained by dividing the TMD lattice constant a_0 by the twist angle θ [4]:

$$a_M \approx \frac{a_0}{\theta}, \tag{9}$$

with $a_0 = 0.328$ nm for WS_2 and θ is an dimensionless variable.

We constructed a hundred sites of the moiré triangular lattices with Eq.8 with Python as shown on Figure 6 (left). The twist angle used in this simulation is $\theta = 2.0^o$, which corresponds to the formation of the valence moiré band in the $WSe_2/MoSe_2$ heterostructure, as previously demonstrated in Ref. [4]. We will vary the twist angle later for more exploration.

The reciprocal vectors are written as:

$$\boldsymbol{b_1} = \frac{2\pi}{a_M}\big(-1,\ \frac{1}{3}\sqrt{3}\big), \tag{10a}$$

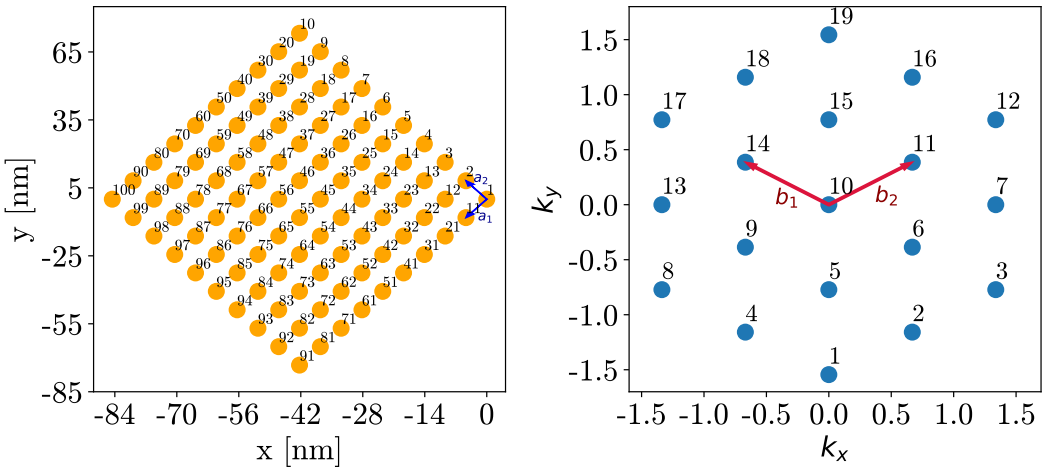

Fig. 6: (left) Representation of TMD moiré triangular lattices in real space with Eq.8, and (right) in a reciprocal space (G-basis) (Eq.10).

$$\boldsymbol{b_2} = \frac{2\pi}{a_M}\left(1,\ \frac{1}{3}\sqrt{3}\right). \tag{10b}$$

Figure 6 (right) presents a depiction of G-basis with 19 reciprocal vectors referred to as the G points, $G(\boldsymbol{b_1}, \boldsymbol{b_2})$.

To define the 1st Brillouin zone, the Wigner-Seitz cell in a reciprocal space, one must draw perpendicular bisectors between the origin (0,0) or G_{10} in this context, with the nearest G point. Figure 7 shows the construction of the 1st Brillouin zone through the mapping of $\boldsymbol{k}$ wave vectors. Using Eq.6, the $\boldsymbol{k}$ wave vectors in Cartesian coordinate is defined by

$$k_x = \frac{i}{N_x}b_{1x} + \frac{j}{N_y}b_{2x}, \tag{11a}$$

$$k_y = \frac{i}{N_x}b_{1y} + \frac{j}{N_y}b_{2y}. \tag{11b}$$

i, j are integers and N_x, N_y are the number of lattice sites in real space with total number of sites $N = N_x \times N_y = 100$, in this case. With $k \equiv |k| = \sqrt{k_x^2 + k_y^2}$, we obtain 100 k points (10×10) as well.

An effective mass of WSe_2 introduced as m^* $0.35m_0$, with m_0 is the free electron mass. We obtain the moiré band Hamiltonian [4]:

$$H = -\frac{\hbar^2\boldsymbol{Q}^2}{2m^*} + \sum_{\boldsymbol{b}} V(\boldsymbol{b})e^{i\boldsymbol{b}\cdot\boldsymbol{r}}. \tag{12}$$

with $\hbar$ is reduced Planck's constant, and $\boldsymbol{Q} = |\boldsymbol{k} + \boldsymbol{G}|$ a momentum. Since the potential is real and each TMD monolayer possesses three-fold rotational symmetry, its value depend on the phase ϕ as shown below (see Figure 8)

$$Vb_1 \equiv V(\boldsymbol{b_1})e^{i\boldsymbol{b}\cdot\boldsymbol{r}} \rightarrow Ve^{i\phi}, \tag{13a}$$

$$Vb_2 \equiv V(\boldsymbol{b_2})e^{i\boldsymbol{b}\cdot\boldsymbol{r}} \rightarrow Ve^{i\phi}, \tag{13b}$$

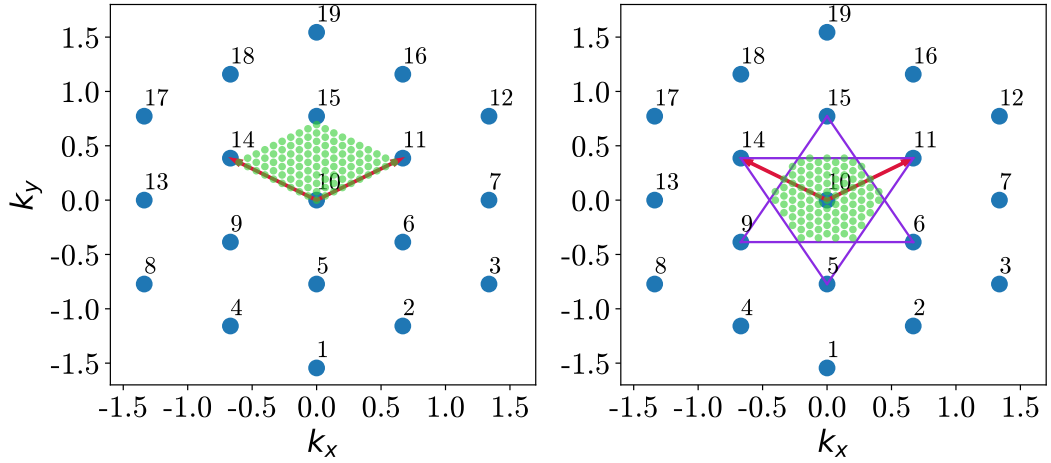

Fig. 7: The 1st Brillouin zone: (left) mapping $\boldsymbol{k}$ wave vectors using Eq.11. (right) distributing the wave vectors within the 1st Brillouin zone by drawing perpendicular bisectors (purple lines perpendicular with $\boldsymbol{b_j}$).

$$Vb_{12} \equiv V(\boldsymbol{b_{12}})e^{i\boldsymbol{b}\cdot\boldsymbol{r}} \rightarrow Ve^{-i\phi}, \tag{13c}$$

with $\boldsymbol{b_{12}} = \boldsymbol{b_1} + \boldsymbol{b_2}$, where the last term on the right was obtained through a Fourier transform.

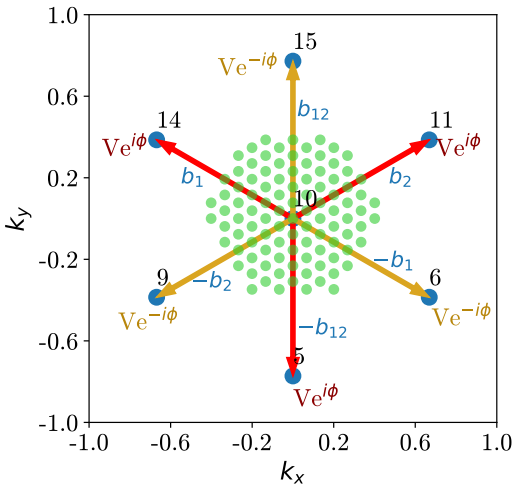

Fig. 8: Potential function in the six nearest neighbors governed by phase function, ϕ, due to the three-fold rotational symmetry of TMD monolayer [4].

Equation 14 below show the Hamiltonian matrix of Eq.12 for 19 G points with $c = -\frac{\hbar^2}{2m^*}$ is a constant. In the off-diagonal part, only the nearest neighbors of each G point have non-zero elements (they have the largest contribution and we neglect farther terms, what is believed to be a good approximation). We can get the energy eigenvalues and eigenvectors by solving this Hamiltonian matrix using the diagonalization method Eq.21 which is introduced in Section 2.2 below. The moiré band of TMD triangular lattice obtained from solving

this Hamiltonian matrix will be discussed in the next section.

$$H = \left(\begin{array}{cccccccc|c} 1 & \cdots & 9 & 10 & 11 & \cdots & 19 & & \\ \hline c|\boldsymbol{k_1}+\boldsymbol{G_1}|^2 & \cdots & 0 & 0 & 0 & \cdots & 0 & & 1 \\ \vdots & \ddots & \vdots & \vdots & \vdots & \cdots & \vdots & & \vdots \\ 0 & \cdots & c|\boldsymbol{k_1}+\boldsymbol{G_9}|^2 & Vb_2 & 0 & \cdots & 0 & & 9 \\ 0 & \cdots & Vb_2* & c|\boldsymbol{k_1}+\boldsymbol{G_{10}}|^2 & Vb2 & \cdots & 0 & & 10 \\ 0 & \cdots & 0 & Vb_2* & c|\boldsymbol{k_1}+\boldsymbol{G_{11}}|^2 & \cdots & 0 & & 11 \\ \vdots & \cdots & \vdots & \vdots & \vdots & \cdots & \vdots & & \vdots \\ 0 & \cdots & 0 & 0 & 0 & \ddots & c|\boldsymbol{k_1}+\boldsymbol{G_{19}}|^2. & & 19 \end{array}\right) \tag{14}$$

2.1.2 Moiré energy band: Continuum model

We compute the valence moiré bands of twisted TMDs by solving the Hamiltonian matrix from Eq.14 using the diagonalization method described in Eq.21, and present the results in Figure 9. The simulation employs 127 G-points and a (21×21) k-point grid, with increased G-points improving the accuracy of the calculations. Fig.9 (left) displays the energy distribution of the highest energy band within the first Brillouin zone for a twist angle of $\theta = 2.0^o$, a phase $\phi = -94^o$ (parameter values from Ref. [4]). V_m is an external voltage that has a significant role to open the gap of the moire band, and in this case, we use $V_m = 11$ meV. The highest band maxima are shown to be concentrated in the Γ regions, indicating the electron density is focused in that area, reaching a value of 10.3 meV, while the minimum value is found at the K-K' edge areas.

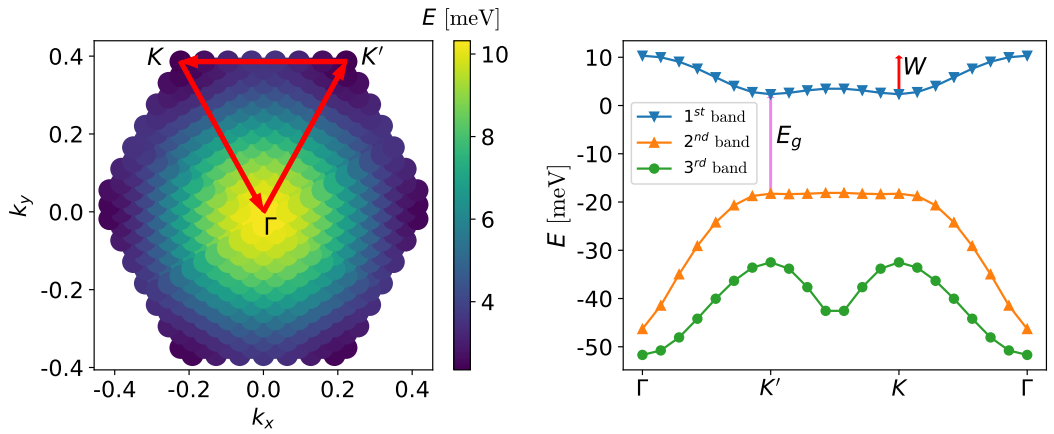

Fig. 9: (left) enerrgy distribution of the 1st maximum energy band in the 1st Brillouin zone (127 G points, (21×21) k-mesh , $\theta = 2.0^o, V = -11\text{meV}, \phi = -94^o$; (right) the 1st, 2nd, and 3rd highest energy band in $\Gamma - K - K' - \Gamma$ regions.

Further analysis focuses on the region under the red arrows, which represent the selected k-points that start from Γ, move to K, then K', and finally return to Γ. This path is used to construct the three highest energy bands of the system as shown in Fig.9 (right). The topmost band (1st band) extrema also can be seen located in the Γ region, with the band width (W) equal to 7.9 meV, representing the energy difference between the maximum and minimum values in the top band. In contrast, the second and third bands exhibit high

energy density in the K-K' regions. The energy gap E_g which is the energy difference between the lowest value in the top band and the highest value in the band below it, is 20.5 meV.

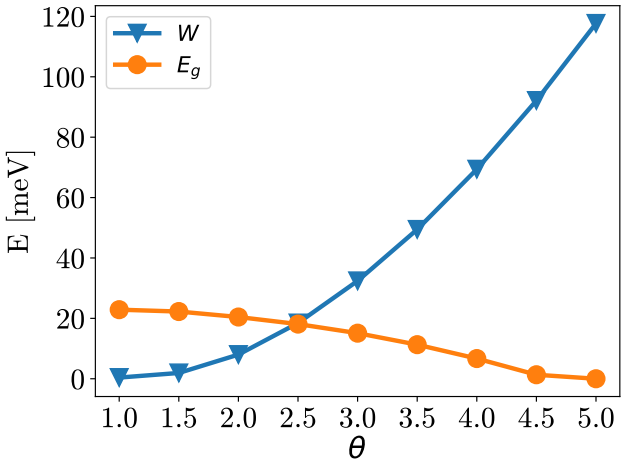

Fig. 10: The width W and bandgap E_g varies as twist angle θ changes.

Figure 10 illustrates how the energy gap E_g varies with changes in the twisted angle θ while keeping other parameters constant. Observations were made only for angles ranging from 1.0^o to 5.0^o. As twist angle increases, the energy gap decreases and reaches nearly zero at $\theta = 5.0^o$, with the maximum energy gap observed at $\theta = 1.0^o$ degrees. Additionally, the band width W increases as twist angle increases. Notable features are observed at a twist angle of 1, where the width is nearly zero. This indicates that the top band is flattened and well-separated from the other bands due to a high energy gap.

2.2 Tight-binding model

Tight-binding models arise by considering two significant properties of crystalline materials [35]: (1) crystals are composed of atoms arranged in a periodic structure, which then produces periodic potentials due to the arrangement of atoms in most stable state; (2) electrons follow Pauli's exclusion, which restricts two electrons with opposite spins from sharing the same energy level. With more electrons in the lattice due to an increase in the number of atoms, it will raise the energy level and the highest level known as Fermi level or valence energy. We can examine the electronic characteristics of crystals at this highest level.

In the lower energy levels, electrons are more tightly bound to atoms, but at the valence level, they are freer, making their kinetic energy dominant while electron-electron interactions become negligible [35]. To describe this valence electron, it is assumed that the electron interacts with the periodic potential but retains the freedom to move by considering the possibility of hopping to neighboring sites. The electron's wave function $|\Psi(\boldsymbol{r}, \boldsymbol{k})\rangle$ can then be expressed as a linear combination $|\Phi(\boldsymbol{r}, \boldsymbol{k})\rangle$ of atomic orbitals $|\phi(\boldsymbol{r})\rangle$, which forms the basis of the tight-binding model.

In a situation where $\boldsymbol{r}$ is similar to the lattice spacing, we need to consider particle-particle interactions, e.g. the Coulomb interaction, and incorporate this as an adjustment $U(\boldsymbol{r})$ to the periodic potential. Then the Hamiltonian of crystal lattice H can be expressed as:

$$H = H_{atom} + U(\boldsymbol{r}), \tag{15}$$

where H_{atom} is the Hamiltonian of localized atom with,

$$H_{atom}|\phi_i(\boldsymbol{r})\rangle = \epsilon_{atom,i}|\phi_i(\boldsymbol{r})\rangle. \tag{16}$$

$\epsilon_{atom,i}$ is the eigenenergy for orbital i.

The solution of Eq.15 must adhere to Bloch's theorem due to the periodic nature of the lattice, by considering the orbital wave function decreases (but not vanishes) as the correction parameter $U(\boldsymbol{r})$ increases. Then the electron's wave function in the lattice system is described by (for further details, see Ref. [35]):

$$|\Psi_j(\boldsymbol{r},\boldsymbol{k})\rangle = \sum C_j|\Phi(\boldsymbol{r},\boldsymbol{k})\rangle. \tag{17}$$

C_j is a complex coefficient and $|\Phi(\boldsymbol{r},\boldsymbol{k})\rangle$ is the Bloch function that expressed with atomic wave function:

$$|\Phi_j(\boldsymbol{r},\boldsymbol{k})\rangle = \frac{1}{\sqrt{N}}\sum_{\boldsymbol{R}} e^{i\boldsymbol{k}\cdot\boldsymbol{r}}|\phi_j(\boldsymbol{r}-\boldsymbol{R})\rangle. \tag{18}$$

N represents the number of primitive cells, $j = 1, \cdots, n$ number of Bloch function, and the exponential part known as phase factor in Bravais lattice.

We can obtain a tight-binding model for a given energy band from a continuum model by using a relation:

$$t_n = \frac{1}{N}\sum_{\boldsymbol{k}} e^{-i\boldsymbol{k}(\boldsymbol{R_i}-\boldsymbol{R_j})}E_k, \tag{19}$$

with E_k are energies of a given energy band obtained from a continuum model shown in Fig. 9. t_n are tight-binding hopping integral given by:

$$t_n = \langle\phi_i|H|\phi_j\rangle = \begin{cases} t_1 = t, & i,j \text{ nearest neighbors} \\ t_2, & i,j \text{ next nearest neighbors} \\ ..., & ... \\ 0, & \text{otherwise.} \end{cases} \tag{20}$$

As the distance between the sites grows, the magnitude of the hopping parameter decreases.

Tight-binding Hamiltonian can be determined by diagonalizing the matrix or solving the secular equation:

$$\det(H - IE) = 0, \tag{21}$$

from the Schrödinger equation:

$$(H - E)|\Psi\rangle = 0.$$

I is identity matrix with the 2D form:

$$I = \begin{pmatrix} 1 & 0 \\ 0 & 1 \end{pmatrix}. \tag{22}$$

This section covers the first quantization approach in the tight-binding model, which describes the system within Hilbert space (using position and momentum). The next section is to discuss the tight-binding model in second quantization, where the system is represented in Fock space using creation and annihilation operators.

For a certain case of a triangular lattice with six nearest neighbor and a nearest neighbor approximation, the energy band is written as:

$$\epsilon_{\boldsymbol{k}}^{tb} = 2t[\cos(\boldsymbol{k}\boldsymbol{a}_1) + \cos(\boldsymbol{k}\boldsymbol{a}_2) + \cos(\boldsymbol{k}\boldsymbol{a}_1 + \boldsymbol{k}\boldsymbol{a}_2)]. \tag{23}$$

2.2.1 Case study for a finite system of 2-site problems

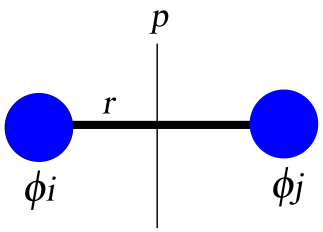

Fig. 11: Illustration parity operator p acts as mirroring...

Solving 2-site problem using parity operator p

The parity operator p is a symmetry operator that reflects the spatial coordinates of a system. A parity operator acts as a reflection operator on a wave function $|\psi\rangle$ (Fig.11)

$$p|\psi\rangle = a|\psi\rangle, \tag{24}$$

with a is a constant. By applying the parity operator, the wave function is classified into symmetric and antisymmetric (even and odd parity) categories. This classification simplifies the process of solving the Schrödinger equation by solving each wave function separately.

If p operates twice on the same $|\psi\rangle$, the wave function is mirroring to its original position:

$$p^2|\psi\rangle = |\psi\rangle = a^2|\psi\rangle. \tag{25}$$

Thus, $a^2 = 1$ is required with possible solutions $a = \pm 1$. Hence from Eq.25 we can write

$$p|\psi\rangle = \pm|\psi\rangle, \tag{26}$$

meaning that after applying the parity operator, the wave function will either remain unchanged (symmetric) or change sign (antisymmetric).

In this section, we demonstrate how to solve a finite system with two-site lattice using the parity operator p. Figure 11 illustrates two sites with their atomic orbitals, $|\phi_1\rangle$ and $|\phi_2\rangle$, separated by a distance r. Since the orbitals are identical, applying the parity operator to $|\phi_1\rangle$ will yield $|\phi_2\rangle$, and vice versa.

The wave function $|\psi\rangle$ for this two-site system is expressed as:

$$|\psi\rangle = c_1|\phi_1\rangle + c_2|\phi_2\rangle, \tag{27}$$

with c_1, c_2 are coefficients. Applying the parity operator to this wave function yields even and odd solutions, as shown in Eq.26. The next step is to analyze these solutions separately.

Positive solution, $|\psi_+\rangle$. Substituting $|\psi\rangle$ in Eq.27 into Eq.26 and focusing on even solution, we write

$$p(c_1|\phi_1\rangle + c_2|\phi_2\rangle) = c_1|\phi_1\rangle + c_2|\phi_2\rangle,$$
$$c_1|\phi_2\rangle + c_2|\phi_1\rangle = c_1|\phi_1\rangle + c_2|\phi_2\rangle = |\psi_+\rangle.$$

From the equation above, we can infer that $c_1 = c_2$, then it becomes $c_1(|\phi_1\rangle + |\phi_2\rangle) = |\psi_+\rangle$. Apply normalization condition,

$$|\psi_{ij}|^2 = \langle\psi_i|\psi_j\rangle = \delta_{ij}, \tag{28}$$

to this wave function $|\psi_+\rangle$ to get the coefficient value of c_1:

$$|\psi_+|^2 = \langle\psi_+|\psi_+\rangle = c_1^* c_1(\langle\phi_1| + \langle\phi_2|)(|\phi_1\rangle + |\phi_2\rangle) = 1,$$
$$c_1^* c_1(\langle\phi_1|\phi_1\rangle + \langle\phi_1|\phi_2\rangle + \langle\phi_2|\phi_1\rangle + \langle\phi_2|\phi_2\rangle).$$

Assuming c_1 is real, then we get the coefficient value $c_1 = \frac{1}{\sqrt{2}}$ and also $c_2 = \frac{1}{\sqrt{2}}$. The final form of the positive solution or symmetric wave function is,

$$|\psi_+\rangle = \frac{1}{\sqrt{2}}(|\phi_1\rangle + |\phi_2\rangle). \tag{29}$$

Negative Solution, $|\psi_-\rangle$. With the same process as in positive solution, the negative solution defined as $|\psi_-\rangle$

$$p(c_1|\phi_1\rangle + c_2|\phi_2\rangle) = -(c_1|\phi_1\rangle + c_2|\phi_2\rangle),$$
$$c_1|\phi_2\rangle + c_2|\phi_1\rangle = -c_1|\phi_1\rangle - c_2|\phi_2\rangle) = |\psi_-\rangle.$$

We can see that $-c_1 = c_2$ and after normalization, the final form of the negative solution or antisymmetric wave function is,

$$|\psi_-\rangle = \frac{1}{\sqrt{2}}(|\phi_1\rangle - |\phi_2\rangle). \tag{30}$$

Solving 2-site problem using diagonalization method

In this section, we will address the same 2-site problem using the diagonalization method (Fig.11). We begin by writing the time-independent Schrödinger equation Eq.2 acts on the wave function $|\psi\rangle$ described in Eq.27:

$$H(c_1|\phi_1\rangle + c_2|\phi_2\rangle) = E(c_1|\phi_1\rangle + c_2|\phi_2\rangle).$$

The next step is to project the equation above using $\langle\phi_1|, \langle\phi_2|$, resulting in two equations:

$$c_1\langle\phi_1|H|\phi_1\rangle + c_2\langle\phi_1|H|\phi_2\rangle = E(c_1\langle\phi_1|\phi_1\rangle + c_2\langle\phi_1|\phi_2\rangle),$$
$$c_1\langle\phi_2|H|\phi_1\rangle + c_2\langle\phi_2|H|\phi_2\rangle = E(c_1\langle\phi_2|\phi_1\rangle + c_2\langle\phi_2|\phi_2\rangle).$$

According to the nearest neighbor rules in Eq.20, we obtain $\langle\phi_i|H|\phi_i\rangle = 0$, $\langle\phi_i|H|\phi_j\rangle = t$, and from the normalization condition in Eq.28, we derive $\langle\phi_i|\phi_i\rangle = 1$, $\langle\phi_i|\phi_j\rangle = 0$. The two equations then become:

$$0 + c_2 t = Ec_1,$$
$$c_1 t + 0 = Ec_2.$$

Express these equations in matrix form as follows:

$$\begin{pmatrix} 0 & t \\ t & 0 \end{pmatrix} \begin{pmatrix} c_1 \\ c_2 \end{pmatrix} = E \begin{pmatrix} c_1 \\ c_2 \end{pmatrix}.$$

The next step is to subtract $E\binom{c_1}{c_2}$ from both sides, then multiplied E with identity matrix Eq.22 obtaining:

$$\begin{pmatrix} -E & t \\ t & -E \end{pmatrix} \begin{pmatrix} c_1 \\ c_2 \end{pmatrix} = 0. \tag{31}$$

By applying the diagonalization method in Eq.21, the energy eigenvalues E are determined by solving:

$$\det \begin{pmatrix} -E & t \\ t & -E \end{pmatrix} = 0.$$

From this point, we arrive at a simple quadratic equation $E^2 - t^2 = 0$ with solutions $E = \pm t$. Next, we need to determine the eigenvectors corresponding to these energy eigenvalues. Since there are two energy eigenvalues ($E = +t$ and $E = -t$), we can find two possible eigenvectors.

First solution: $E = +t$. Subtitute $E = t$ into Eq.31, then perform the matrix multiplication to get:

$$-tc_1 + tc_2 = 0 \quad \cdots(a),$$
$$tc_1 - tc_2 = 0 \quad \cdots(b).$$

The two equations are equivalent. From equation (a), we find that $-c_1 + c_2 = 0$, which implies $c_1 = c_2$. Substitute this into the wave function Eq.27:

$$|\psi\rangle = c_1(|\phi_1\rangle + |\phi_2\rangle).$$

After normalizing the wave function with Eq.28, the final expression for the eigen wave function for $E = +t$ is

$$|\psi\rangle = \frac{1}{\sqrt{2}}(|\phi_1\rangle + |\phi_2\rangle),$$

which is the same as the Positive solution $|\psi_+\rangle$ Eq.29.

Second solution: $E = -t$**.** The same procedure is applied here as in the First solution, but with $E = -t$ substituted into Eq.31:

$$\begin{pmatrix} t & t \\ t & t \end{pmatrix} \begin{pmatrix} c_1 \\ c_2 \end{pmatrix} = 0.$$

By solving this, we find $c_1 = -c_2$. Substituting this value into the wave function yields $|\psi\rangle = c_1(|\phi_1\rangle - |\phi_2\rangle)$. After the normalization the eigen wave function is:

$$|\psi\rangle = \frac{1}{\sqrt{2}}(|\phi_1\rangle - |\phi_2\rangle),$$

which matches the Negative solution $|\psi_-\rangle$ from Eq.30.

2.2.2 Moiré energy band: Tight-binding model

In this section, we extend our analysis from Section 2.1.2 by using a transformation between a continuum model and a tight-binding model. To calculate the energy of the TMDs lattice we take the following parameters: $\phi = -94^o, \theta = 2.0^o$, and $V_m = -11$ meV. We map the top band to the tight-binding model from Eq.34, incorporating the hopping parameters for the first t_1, second t_2, and third t_3 nearest neighbors, as shown in Figure 12. Except when the parameter becomes the independent variable on the x-axis, the values remain constant. The energy band aligns well with the continuum model, with a slight variation due to the correction of the hopping energy of electrons (see Figure 12). The hopping energy changes with the external voltage V_m. As the voltage increases and widens the bandgap, it becomes more difficult for electrons to hop between energy bands or requires more energy to do so. In Figure 12 (upper-right), the highest hopping energy occurs when there is no external voltage ($V_m = 0$) because, at that point, the moiré band has no bandgap.

As the twist angle increases, the hopping energy also rises. A larger twist angle reduces the moiré pattern size, increasing wavefunction overlap and facilitating electron transitions between different patterns. Additionally, hopping energy rises with increasing width, consistent with the previous analysis of W and the band gap. A smaller width indicates a flatter band with a larger bandgap. Since hopping energy relates to the kinetic energy required for electron movement, smaller twist angles create a larger moiré pattern, leading to more electron localization in the AA region. We also observed that the first nearest neighbor obtained a much greater impact in this analysis compared to the second and third nearest neighbors.

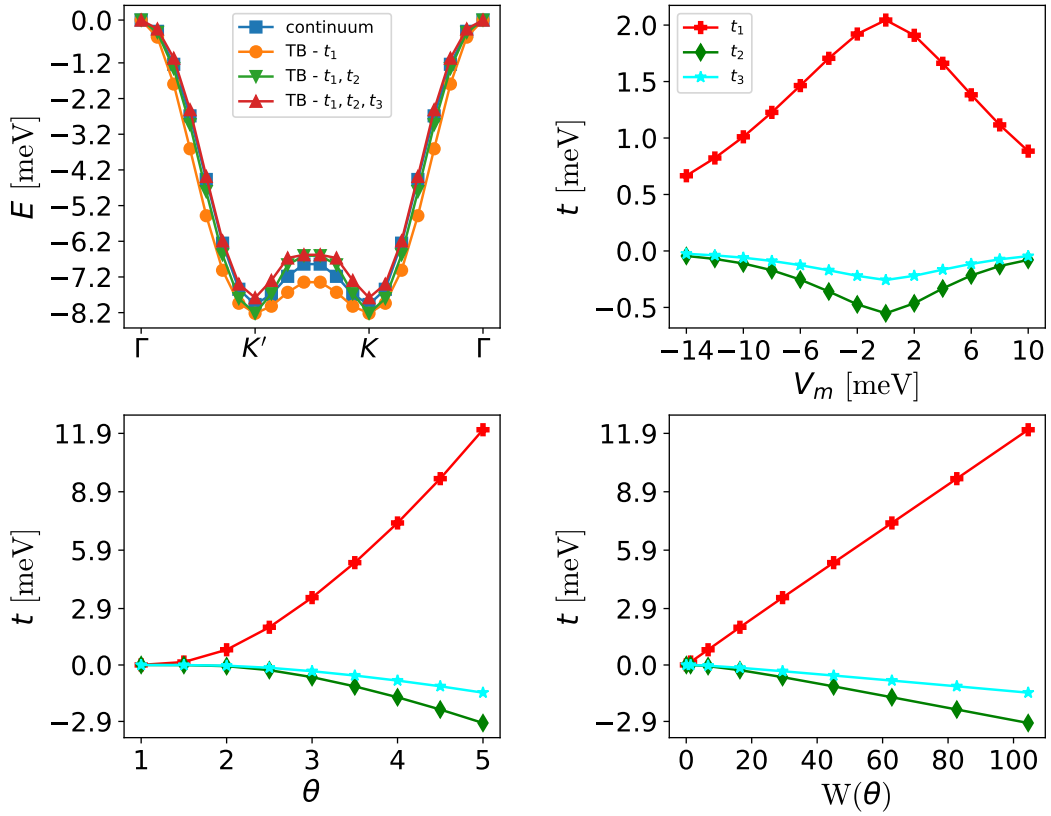

Fig. 12: The observation of the tight-binding approach on the top band takes into account the first, second, and third nearest neighbors (t_1, t_2, and t_3). Additionally, we demonstrate how the hopping energy changes with variations in voltage V_m, twist angle θ, and width W.

2.2.3 Second quantization

Second quantization emphasizes the quantization of fields by considering particles as excitations of these fields, and it is represented using creation and annihilation operators ($c^\dagger$ and c) used to add or remove electrons in vacant states $|0\rangle$ [36]:

$$c|0\rangle = 0, \tag{32a}$$

$$\langle 0|c^\dagger = 0. \tag{32b}$$

Operator $c^\dagger$ and c obey the commutation rules for fermions:

$$\{c_i^\dagger, c_j^\dagger\} = c_i^\dagger c_j^\dagger + c_j^\dagger c_i^\dagger = 0, \tag{33a}$$

$$\{c_i, c_j\} = c_i c_j + c_j c_i = 0, \tag{33b}$$

$$\{c_i, c_j^\dagger\} = c_i c_j^\dagger + c_j^\dagger c_i = \delta_{ij}, \tag{33c}$$

$$\{c_{i\sigma}, c_{j\sigma\prime}\} = 0, \tag{33d}$$

$$\{c_{i\sigma}, c_{j\sigma\prime}^\dagger\} = \delta_{ij}\delta_{\sigma\sigma\prime}, \tag{33e}$$

with i, j describe states and $\sigma, \sigma\prime$ describe the spin orientation (e.g. $\uparrow$ or $\downarrow$).

The Hamiltonian Eq.15 then must be expressed using these operators. The tight-binding Hamiltonian in second quantization has already been derived as [35]:

$$H_{tb} = \sum_{ij} \langle i|H|j\rangle c_{ij}^{\dagger} c_{ij}, \tag{34}$$

i, j are the states in Hilbert space basis with $\langle i|H|j\rangle = \langle \phi_i|H|\phi_j\rangle = t$ related to hopping integral.

2.3 Many-body Hamiltonian and Hubbard model

The many-body Hamiltonian represents the total energy of a system with multiple interacting particles. General many-body Hamiltonian has a form [34]:

$$H = \sum_{ij\sigma} t_{ij} c_{i\sigma}^{\dagger} c_{i\sigma} + \frac{1}{2} \sum_{ijkl\sigma\sigma'} \langle ij|v|kl\rangle c_{i\sigma}^{\dagger} c_{j\sigma\prime}^{\dagger} c_{k\sigma\prime} c_{l\sigma} = H_0 + H_c \tag{35}$$

where the Coulomb potential is described by,

$$\langle ij|v|kl\rangle = \iint d\vec{r} d\vec{r\prime} \frac{\phi_i^*(\vec{r})\phi_j^*(\vec{r\prime})\phi_k(\vec{r\prime})\phi_l(\vec{r})}{|\vec{r} - \vec{r\prime}|} \tag{36}$$

Hamiltonian given by Eq.35 commutes with projection of spin on z axis operator, spin S_z,

$$S_z = \frac{1}{2}(N_{\uparrow} - N_{\downarrow}). \tag{37}$$

Many-body Hamiltonian commutes also with total spin operator,

$$[S^2, H] = 0, \tag{38}$$

which allows one to determine magnetic properties of the ground state.

Hubbard models describe the behavior of valence electrons in a crystal lattice by combining kinetic energy, represented by hopping parameters as in tight-binding models, with Coulomb interaction. We can consider different versions of Hubbard model, generalized Hubbard model, extended Hubbard model, and the simplest version, on-site Hubbard model (which is called Hubbard model). The generalized Hubbard model is given by 35 with restriction of Coulomb matrix elements $\langle ij|v|kl\rangle$ to nonzero terms for $U = \langle ii|v|ii\rangle$, $D = \langle ij|v|ji\rangle$, $X = \langle ij|v|ij\rangle$, $A = \langle ii|v|ij\rangle$ [37,38]. For Hubbard model, only on-site repulsion is nonzero, $U = \langle ii|v|ii\rangle$, and can be written as:

$$H = \sum_{ij\sigma} t_{ij} c_{i\sigma}^{\dagger} c_{j\sigma} + U \sum_{i} c_{i\downarrow}^{\dagger} c_{i\downarrow} c_{i\uparrow}^{\dagger} c_{i\uparrow}. \tag{39}$$

2.3.1 Solving 2-site many-body problem with two particles using Exact Diagonalization method

Figure 13 below show the electron configurations for two-site two-particle systems. There are six possible configuration states in this case, with each state

can be represented with creation $(c_1^\dagger, c_2^\dagger)$ operator (index $1, 2$ denoted the number of a site) operating with unoccupied or vacuum state $|0\rangle$. For simplicity $|\psi_i\rangle = |i\rangle$; where $i = 0, 1, 2, ...$, and notiation for electron spin up $= \uparrow$ with spin down $= \downarrow$.

$\downarrow$	$\downarrow$	$\|1\rangle = c_{1\downarrow}^\dagger c_{2\downarrow}^\dagger \|0\rangle$
$\uparrow$	$\uparrow$	$\|2\rangle = c_{1\uparrow}^\dagger c_{2\uparrow}^\dagger \|0\rangle$
$\downarrow$	$\uparrow$	$\|3\rangle = c_{1\downarrow}^\dagger c_{2\uparrow}^\dagger \|0\rangle$
$\uparrow$	$\downarrow$	$\|4\rangle = c_{1\uparrow}^\dagger c_{2\downarrow}^\dagger \|0\rangle$
$\downarrow\uparrow$		$\|5\rangle = c_{1\downarrow}^\dagger c_{1\uparrow}^\dagger \|0\rangle$
	$\downarrow\uparrow$	$\|6\rangle = c_{2\downarrow}^\dagger c_{2\uparrow}^\dagger \|0\rangle$

Fig. 13: Two-site two-particle problem with the configuration states.

To solve the two-site system, we must find nonzero matrix elements $\langle i|H|j\rangle = \langle\phi_i|H|\phi_j\rangle$, where a many body wavefunciton is $|\psi\rangle = \sum_i A_i|\phi_i\rangle$ and A_i are unknown coefficients. The objective is to determine the Hamiltonian matrix. We begin by splitting the Hamiltonian as shown in Eq.35 and then calculate it step by step for each state, from $|1\rangle$ to $|6\rangle$. Starting with $|1\rangle$, we project it with $\langle\phi_1| = \langle 1|$:

$$\langle 1|H|1\rangle = \langle 1|H_0|1\rangle + \langle 1|H_c|1\rangle.$$

Let's start by solving the first sequence:

$$\begin{aligned}\langle 1|H_0|1\rangle &= \sum_{ij\sigma} t_{ij}\langle 0|c_{2\downarrow}c_{1\downarrow}c_{i\sigma}^\dagger c_{j\sigma}c_{1\downarrow}^\dagger c_{2\downarrow}^\dagger|0\rangle \\ &= t_{12}\langle 0|c_{2\downarrow}c_{1\downarrow}c_{1\uparrow}^\dagger c_{2\uparrow}c_{1\downarrow}^\dagger c_{2\downarrow}^\dagger|0\rangle + t_{12}\langle 0|c_{2\downarrow}c_{1\downarrow}c_{1\downarrow}^\dagger c_{2\downarrow}c_{1\downarrow}^\dagger c_{2\downarrow}^\dagger|0\rangle \\ &\quad + t_{21}\langle 0|c_{2\downarrow}c_{1\downarrow}c_{2\uparrow}^\dagger c_{1\uparrow}c_{1\downarrow}^\dagger c_{2\downarrow}^\dagger|0\rangle + t_{21}\langle 0|c_{2\downarrow}c_{1\downarrow}c_{2\downarrow}^\dagger c_{1\downarrow}c_{1\downarrow}^\dagger c_{2\downarrow}^\dagger|0\rangle.\end{aligned}$$

The summation goes up to 2 because we are dealing with a 2-site system. The result simplifies to only 4 sequences due to $i \neq j$ (since $t_{ii} = t_{jj} = 0$). Now, solve each sequence individually, beginning with the first sequence where $i = 1, j = 2$, and $\sigma = \uparrow$:

$$t_{12}\langle 0|c_{2\downarrow}c_{1\downarrow}c_{1\uparrow}^\dagger c_{2\uparrow}c_{1\downarrow}^\dagger c_{2\downarrow}^\dagger|0\rangle.$$

To solve this, we need to move the annihilation operator to the right, where it acts on $|0\rangle$, and move the creation operator to act on $\langle 0|$. This can be done by applying the commutation rules for fermions Eq.33.

Consider c_2, we want to move this operator to the right by swapping it with $c_1^\dagger$ using the rules from Eq.33c, resulting in $c_{2\uparrow}c_{1\downarrow}^\dagger = -c_{1\downarrow}^\dagger c_{2\uparrow}$. Then, switch $c_{2\uparrow}$ with $c_{2\downarrow}^\dagger$ according to Eq.33d (introducing a negative sign once more). This gives us:

$$t_{12}\langle 0|c_{2\downarrow}c_{1\downarrow}c_{1\uparrow}^\dagger \boldsymbol{c_{2\uparrow}} c_{1\downarrow}^\dagger c_{2\downarrow}^\dagger|0\rangle = t_{12}\langle 0|c_{2\downarrow}c_{1\downarrow}c_{1\uparrow}^\dagger c_{1\downarrow}^\dagger c_{2\downarrow}^\dagger \boldsymbol{c_{2\uparrow}}|0\rangle = 0.$$

We obtained zero from the above equation, as indicated by Eq.32a. Repeating the same steps for the second, third, and fourth sequences and applying the commutation rules yields:

$$t_{12}\langle 0|c_{2\downarrow}c_{1\downarrow}c^{\dagger}_{1\downarrow}c_{2\downarrow}c^{\dagger}_{1\downarrow}c^{\dagger}_{2\downarrow}|0\rangle = 0,$$
$$t_{21}\langle 0|c_{2\downarrow}c_{1\downarrow}c^{\dagger}_{2\uparrow}c_{1\uparrow}c^{\dagger}_{1\downarrow}c^{\dagger}_{2\downarrow}|0\rangle = 0,$$
$$t_{21}\langle 0|c_{2\downarrow}c_{1\downarrow}c^{\dagger}_{2\downarrow}c_{1\downarrow}c^{\dagger}_{1\downarrow}c^{\dagger}_{2\downarrow}|0\rangle = 0.$$

Therefore, summing up all the sequences gives $\langle 1|H_0|1\rangle = 0$. Next, project $H_0|1\rangle$ again with $\langle 2|, \langle 3|, \langle 4|, \langle 5|$, and $\langle 6|$.

Since the two-site with two-particle problem has six configuration states, we need to perform the same calculation of H_0 as above for $|2\rangle, |3\rangle, |4\rangle, |5\rangle, |6\rangle$ and projected them. This will give us the (6×6) Hamiltonian matrix for H_0:

$$H_0 = \begin{pmatrix} 0 & 0 & 0 & 0 & 0 & 0 \\ 0 & 0 & 0 & 0 & 0 & 0 \\ 0 & 0 & 0 & 0 & t_{21} & t_{12} \\ 0 & 0 & 0 & 0 & -t_{21} & -t_{12} \\ 0 & 0 & t_{12} & -t_{12} & 0 & 0 \\ 0 & 0 & t_{21} & -t_{21} & 0 & 0 \end{pmatrix}. \tag{40}$$

This H_0 corresponds to the kinetic energy of the particles, as described by the hopping parameter t.

Next, solve H_c as given in Equation 35, beginning with the evaluation of $\langle 1|H_c|1\rangle$:

$$\langle 1|H_c|1\rangle = \sum_{ijkl,\sigma\sigma\prime} v_{ijkl}\langle 0|c_{2\downarrow}c_{1\downarrow}c^{\dagger}_{i\sigma}c^{\dagger}_{j\sigma\prime}c_{k\sigma\prime}c_{l\sigma}c^{\dagger}_{1\downarrow}c^{\dagger}_{2\downarrow}|0\rangle.$$

Similar to H_0, the summation in H_c goes up to 2 meaning the indices i, j, k, and l are either 1 or 2. Consequently, we will encounter longer sequences compared to H_0. Starting with $i = k = 1$ and $j = l = 2$, we obtain $v_{ijji} = v_{1221}$ for all possible spin values σ and $\sigma\prime$:

$$\begin{aligned} v_{1221}\langle 0|c_{2\downarrow}c_{1\downarrow}c^{\dagger}_{1\sigma}c^{\dagger}_{2\sigma\prime}c_{2\sigma\prime}c_{1\sigma}c^{\dagger}_{1\downarrow}c^{\dagger}_{2\downarrow}|0\rangle = {} & v_{1221}\langle 0|c_{2\downarrow}c_{1\downarrow}c^{\dagger}_{1\uparrow}c^{\dagger}_{2\uparrow}c_{2\uparrow}c_{1\uparrow}c^{\dagger}_{1\downarrow}c^{\dagger}_{2\downarrow}|0\rangle \\ & + v_{1221}\langle 0|c_{2\downarrow}c_{1\downarrow}c^{\dagger}_{1\uparrow}c^{\dagger}_{2\downarrow}c_{2\downarrow}c_{1\uparrow}c^{\dagger}_{1\downarrow}c^{\dagger}_{2\downarrow}|0\rangle \\ & + v_{1221}\langle 0|c_{2\downarrow}c_{1\downarrow}c^{\dagger}_{1\downarrow}c^{\dagger}_{2\uparrow}c_{2\uparrow}c_{1\downarrow}c^{\dagger}_{1\downarrow}c^{\dagger}_{2\downarrow}|0\rangle \\ & + v_{1221}\langle 0|c_{2\downarrow}c_{1\downarrow}c^{\dagger}_{1\downarrow}c^{\dagger}_{2\downarrow}c_{2\downarrow}c_{1\downarrow}c^{\dagger}_{1\downarrow}c^{\dagger}_{2\downarrow}|0\rangle. \end{aligned}$$

We need to solve these four sequences. The first sequence ($\sigma = \sigma\prime = \uparrow$) and the second sequence ($\sigma = \uparrow, \sigma\prime = \downarrow$) can be easily solved by moving the annihilation operator $c_{1\uparrow}$ to the right to act on $|0\rangle$, as done in solving H_0. Both sequences result in zero.

For the third sequence ($\sigma = \downarrow, \sigma\prime = \uparrow$), we need to swap $c_{1\downarrow}$ with $c^{\dagger}_{1\downarrow}$ by using commutation rule Eq.33e.

$$c_{1\downarrow}, c^{\dagger}_{1\downarrow} = c_{1\downarrow}c^{\dagger}_{1\downarrow} + c^{\dagger}_{1\downarrow}c_{1\downarrow} = 1 \rightarrow c_{1\downarrow}c^{\dagger}_{1\downarrow} = 1 - c^{\dagger}_{1\downarrow}c_{1\downarrow}.$$

Substituting this into the third sequence will divide it into two separate sequences. Then, as usual, move the annihilation operator to act on the vacuum state. The process is described as follows:

$$\begin{aligned}
v_{1221}\langle 0|c_{2\downarrow}c_{1\downarrow}c_{1\downarrow}^{\dagger}c_{2\uparrow}^{\dagger}c_{2\uparrow}\boldsymbol{c_{1\downarrow}c_{1\downarrow}^{\dagger}}c_{2\downarrow}^{\dagger}|0\rangle &= v_{1221}\langle 0|c_{2\downarrow}c_{1\downarrow}c_{1\downarrow}^{\dagger}c_{2\uparrow}^{\dagger}c_{2\uparrow}(1-\boldsymbol{c_{1\downarrow}^{\dagger}c_{1\downarrow}})c_{2\downarrow}^{\dagger}|0\rangle \\
&= v_{1221}\langle 0|c_{2\downarrow}c_{1\downarrow}c_{1\downarrow}^{\dagger}c_{2\uparrow}^{\dagger}\boldsymbol{c_{2\uparrow}}(1)c_{2\downarrow}^{\dagger}|0\rangle \\
&\quad - v_{1221}\langle 0|c_{2\downarrow}c_{1\downarrow}c_{1\downarrow}^{\dagger}c_{2\uparrow}^{\dagger}c_{2\uparrow}(c_{1\downarrow}^{\dagger}\boldsymbol{c_{1\downarrow}})c_{2\downarrow}^{\dagger}|0\rangle \\
&= -v_{1221}\langle 0|c_{2\downarrow}c_{1\downarrow}c_{1\downarrow}^{\dagger}c_{2\uparrow}^{\dagger}c_{2\downarrow}^{\dagger}\boldsymbol{c_{2\uparrow}}|0\rangle \\
&\quad + v_{1221}\langle 0|c_{2\downarrow}c_{1\downarrow}c_{1\downarrow}^{\dagger}c_{2\uparrow}^{\dagger}c_{2\uparrow}c_{1\downarrow}^{\dagger}c_{2\downarrow}^{\dagger}\boldsymbol{c_{1\downarrow}}|0\rangle \\
&= 0.
\end{aligned}$$

In the fourth sequence, begin by swapping the two pairs of $c_{1\downarrow}$ and $c_{1\downarrow}^{\dagger}$:

$$\begin{aligned}
v_{1221}\langle 0|c_{2\downarrow}\boldsymbol{c_{1\downarrow}c_{1\downarrow}^{\dagger}}c_{2\downarrow}^{\dagger}c_{2\downarrow}\boldsymbol{c_{1\downarrow}c_{1\downarrow}^{\dagger}}c_{2\downarrow}^{\dagger}|0\rangle &= v_{1221}\langle 0|c_{2\downarrow}(1-\boldsymbol{c_{1\downarrow}^{\dagger}c_{1\downarrow}})c_{2\downarrow}^{\dagger}c_{2\downarrow}(1-\boldsymbol{c_{1\downarrow}^{\dagger}c_{1\downarrow}})c_{2\downarrow}^{\dagger}|0\rangle \\
&= v_{1221}\langle 0|c_{2\downarrow}(1)c_{2\downarrow}^{\dagger}c_{2\downarrow}(1)c_{2\downarrow}^{\dagger}|0\rangle \\
&\quad - v_{1221}\langle 0|c_{2\downarrow}(1)c_{2\downarrow}^{\dagger}c_{2\downarrow}(\boldsymbol{c_{1\downarrow}^{\dagger}c_{1\downarrow}})c_{2\downarrow}^{\dagger}|0\rangle \\
&\quad - v_{1221}\langle 0|c_{2\downarrow}(\boldsymbol{c_{1\downarrow}^{\dagger}c_{1\downarrow}})c_{2\downarrow}^{\dagger}c_{2\downarrow}(1)c_{2\downarrow}^{\dagger}|0\rangle \\
&\quad + v_{1221}\langle 0|c_{2\downarrow}(\boldsymbol{c_{1\downarrow}^{\dagger}c_{1\downarrow}})c_{2\downarrow}^{\dagger}c_{2\downarrow}(\boldsymbol{c_{1\downarrow}^{\dagger}c_{1\downarrow}})c_{2\downarrow}^{\dagger}|0\rangle.
\end{aligned}$$

As usual, moving the annihilation operator to act on $|0\rangle$ or moving the creation operator to act on $\langle 0|$ in the second, third, and fourth sequences results in zero. This leaves only the first sequence remaining:

$$\begin{aligned}
v_{1221}\langle 0|c_{2\downarrow}c_{1\downarrow}c_{1\downarrow}^{\dagger}c_{2\downarrow}^{\dagger}c_{2\downarrow}c_{1\downarrow}c_{1\downarrow}^{\dagger}c_{2\downarrow}^{\dagger}|0\rangle &= v_{1221}\langle 0|c_{2\downarrow}c_{2\downarrow}^{\dagger}c_{2\downarrow}c_{2\downarrow}^{\dagger}|0\rangle \\
&\quad + v_{1221}\langle 0|\boldsymbol{c_{2\downarrow}^{\dagger}}c_{2\downarrow}c_{2\downarrow}c_{1\downarrow}^{\dagger}c_{1\downarrow}c_{2\downarrow}^{\dagger}|0\rangle \\
&\quad + v_{1221}\langle 0|\boldsymbol{c_{1\downarrow}^{\dagger}}c_{2\downarrow}c_{1\downarrow}c_{2\downarrow}^{\dagger}c_{2\downarrow}c_{2\downarrow}^{\dagger}|0\rangle \\
&\quad - v_{1221}\langle 0|\boldsymbol{c_{2\downarrow}}c_{1\downarrow}^{\dagger}c_{1\downarrow}c_{2\downarrow}^{\dagger}c_{2\downarrow}c_{1\downarrow}^{\dagger}c_{1\downarrow}c_{2\downarrow}^{\dagger}|0\rangle \\
&= v_{1221}\langle 0|c_{2\downarrow}c_{2\downarrow}^{\dagger}c_{2\downarrow}c_{2\downarrow}^{\dagger}|0\rangle + 0 + 0 - 0 \\
&= v_{1221}\langle 0|c_{2\downarrow}c_{2\downarrow}^{\dagger}c_{2\downarrow}c_{2\downarrow}^{\dagger}|0\rangle.
\end{aligned}$$

Again, by using Eq.33e:

$$\begin{aligned}
v_{1221}\langle 0|c_{2\downarrow}c_{1\downarrow}c_{1\downarrow}^{\dagger}c_{2\downarrow}^{\dagger}c_{2\downarrow}c_{1\downarrow}c_{1\downarrow}^{\dagger}c_{2\downarrow}^{\dagger}|0\rangle &= v_{1221}\langle 0|(1-c_{2\downarrow}^{\dagger}c_{2\downarrow})(1-c_{2\downarrow}^{\dagger}c_{2\downarrow})|0\rangle \\
&= v_{1221}\langle 0|0\rangle - v_{1221}\langle 0|c_{2\downarrow}^{\dagger}c_{2\downarrow}|0\rangle \\
&\quad - v_{1221}\langle 0|c_{2\downarrow}^{\dagger}c_{2\downarrow}|0\rangle + v_{1221}\langle 0|c_{2\downarrow}^{\dagger}c_{2\downarrow}c_{2\downarrow}^{\dagger}c_{2\downarrow}|0\rangle \\
&= v_{1221} - 0 - 0 + 0 \\
&= v_{1221}
\end{aligned}$$

This result corresponds to $i = l = 1$ and $j = k = 2$. Next, substitute various combinations i, j, k, l to obtain values. Typically, this is done for U, D, X, and

A in the generalized Hubbard model given in Eq.39:

$$\begin{aligned}\langle ii|v|ii\rangle &= v_{iiii} = U,\\ \langle ij|v|ji\rangle &= v_{ijji} = D,\\ \langle ij|v|ij\rangle &= v_{ijij} = X,\\ \langle ii|v|ij\rangle &= v_{iiij} = A.\end{aligned}$$

Perform the calculation for all states to obtain the matrix H_c, which represents the energy of particle-particle interactions.

$$H_c = \begin{pmatrix} (D-X) & 0 & 0 & 0 & 0 & 0\\ 0 & (D-X) & 0 & 0 & 0 & 0\\ 0 & 0 & D & -X & A & A\\ 0 & 0 & -X & D & -A & -A\\ 0 & 0 & A & -A & U & 0\\ 0 & 0 & A & -A & 0 & U \end{pmatrix}. \tag{41}$$

Combine H_0 and H_c to get the final form of the matrix H:

$$H = \begin{pmatrix} (D-X) & 0 & 0 & 0 & 0 & 0\\ 0 & (D-X) & 0 & 0 & 0 & 0\\ 0 & 0 & D & -X & (t_{21}+A) & (t_{12}+A)\\ 0 & 0 & -X & D & -(t_{21}+A) & -(t_{12}+A)\\ 0 & 0 & (t_{12}+A) & -(t_{12}+A) & U & 0\\ 0 & 0 & (t_{21}+A) & -(t_{21}+A) & 0 & U \end{pmatrix}.$$

We can see the Hamiltonian matrix above consists of a small matrix (2×2) in row (and column) 1 to 2, and matrix (4×4) in row 3 to 6. Now, let's introduce a new state that consists of a combination of states Fig.13.

$$\begin{array}{ccccccc} \underline{\downarrow\uparrow} & \underline{\quad\quad} & + & \underline{\quad\quad} & \underline{\downarrow\uparrow} & \quad |5\prime\rangle = \frac{1}{\sqrt{2}}(|5\rangle + |6\rangle)\\ \underline{\downarrow\uparrow} & \underline{\quad\quad} & - & \underline{\quad\quad} & \underline{\downarrow\uparrow} & \quad |6\prime\rangle = \frac{1}{\sqrt{2}}(|5\rangle - |6\rangle) \end{array}$$

Fig. 14: Introduce two new states which are the linear combination of original states $|5\rangle, |6\rangle$.

Figure 14 shows two new states $(|5\prime\rangle, |6\prime\rangle)$ which is constructed by adding and subtracting $|5\rangle$ with $|6\rangle$. Project these state with $\langle 1|, \langle 2|, \langle 3|, \langle 4|, \langle 5\prime|$, and $\langle 6\prime|$. Here below we show the calculation for operator H_c acts on $\langle 5\prime|$, $\langle 6\prime|$ and both projected on $\langle 3|$:

$$\begin{aligned}\langle 3|H_c|5\prime\rangle &= \frac{1}{\sqrt{2}}(\langle 3|H_c|5\rangle + \langle 3|H_c|6\rangle),\\ \langle 3|H_c|6\prime\rangle &= \frac{1}{\sqrt{2}}(\langle 3|H_c|5\rangle - \langle 3|H_c|6\rangle).\end{aligned}$$

We already have results for the right-hand components in Eq.41. By inserting these value, we got:

$$\begin{aligned}\langle 3|H_c|5\prime\rangle &= \frac{1}{\sqrt{2}}(A+A) = \frac{2}{\sqrt{2}}A,\\ \langle 3|H_c|6\prime\rangle &= \frac{1}{\sqrt{2}}(A-A) = 0.\end{aligned}$$

Hence, the final form of H_c becomes:

$$H_c = \begin{pmatrix} |1\rangle & |2\rangle & |3\rangle & 4\rangle & |5\prime\rangle & |6\prime\rangle & \\ (D-X) & 0 & 0 & 0 & 0 & 0 & \langle 1| \\ 0 & (D-X) & 0 & 0 & 0 & 0 & \langle 2| \\ 0 & 0 & D & -X & \sqrt{2}A & 0 & \langle 3| \\ 0 & 0 & -X & D & -\sqrt{2}A & 0 & \langle 4| \\ 0 & 0 & \sqrt{2}A & -\sqrt{2}A & U & 0 & \langle 5\prime| \\ 0 & 0 & 0 & 0 & 0 & U. & \langle 6\prime| \end{pmatrix} \tag{42}$$

The non-diagonal values in matrix (4×4) are change comparing to the previous result in H_c in Eq.41, and non-diagonal part of row and column $|6\prime\rangle$ all zero. From here we can see that the matrix (4×4) is reduced into a matrix (3×3).

Again, let's introduce new states by combining $|3\rangle$ and $|4\rangle$ as shown in Fiq.15 below: With the same procedure, project these new states $(|3\prime\rangle, |4\rangle)$ with

$$\begin{array}{cccc} \downarrow & \uparrow & + & \uparrow \quad \downarrow \\ \hline \downarrow & \uparrow & - & \uparrow \quad \downarrow \end{array} \qquad \begin{array}{l} |3\prime\rangle = \frac{1}{\sqrt{2}}(|3\rangle + |4\rangle) \\ |4\prime\rangle = \frac{1}{\sqrt{2}}(|3\rangle - |4\rangle) \end{array}$$

Fig. 15: Introduce two new states which are the linear combination of original states $|3\rangle, |4\rangle$.

$\langle 1|, \langle 2|, \langle 3\prime|, \langle 4\prime|, \langle 5\prime|$, and $\langle 6\prime|$. Here we only show the calculation of H_c acts on $|3\prime\rangle$ and projected on $\langle 4\prime|$.

$$\begin{aligned} \langle 4\prime|H_c|3\prime\rangle &= \frac{1}{\sqrt{2}}(\langle 4\prime|H_c|3\rangle + \langle 4\prime|H_c|4\rangle) \\ &= \frac{1}{\sqrt{2}}\frac{1}{\sqrt{2}}(\langle 3|H_c|3\rangle - \langle 4|H_c|3\rangle + \langle 3|H_c|4\rangle - \langle 4|H_c|4\rangle). \end{aligned}$$

Use values of the current H_c matrix in Eq.42:

$$\langle 4\prime|H_c|3\prime\rangle = \frac{1}{2}(D + X - X - D) = 0.$$

After calculating all components we have the newest H_c matrix:

$$H_c = \begin{pmatrix} |1\rangle & |2\rangle & |3\prime\rangle & 4\prime\rangle & |5\prime\rangle & |6\prime\rangle & \\ (D-X) & 0 & 0 & 0 & 0 & 0 & \langle 1| \\ 0 & (D-X) & 0 & 0 & 0 & 0 & \langle 2| \\ 0 & 0 & (D-X) & 0 & 0 & 0 & \langle 3\prime| \\ 0 & 0 & 0 & (D+X) & 2A & 0 & \langle 4\prime| \\ 0 & 0 & 0 & 2A & U & 0 & \langle 5\prime| \\ 0 & 0 & 0 & 0 & 0 & U. & \langle 6\prime| \end{pmatrix}$$

Take a look in the matrix (4×4) area which was already reduced into matrix (3×3) in the previous calculation, now it is again reduced into a simpler matrix (2×2).

In this study, we examine many-body problems by addressing strong electron correlations in a finite-sized twisted moiré triangular lattice. We construct

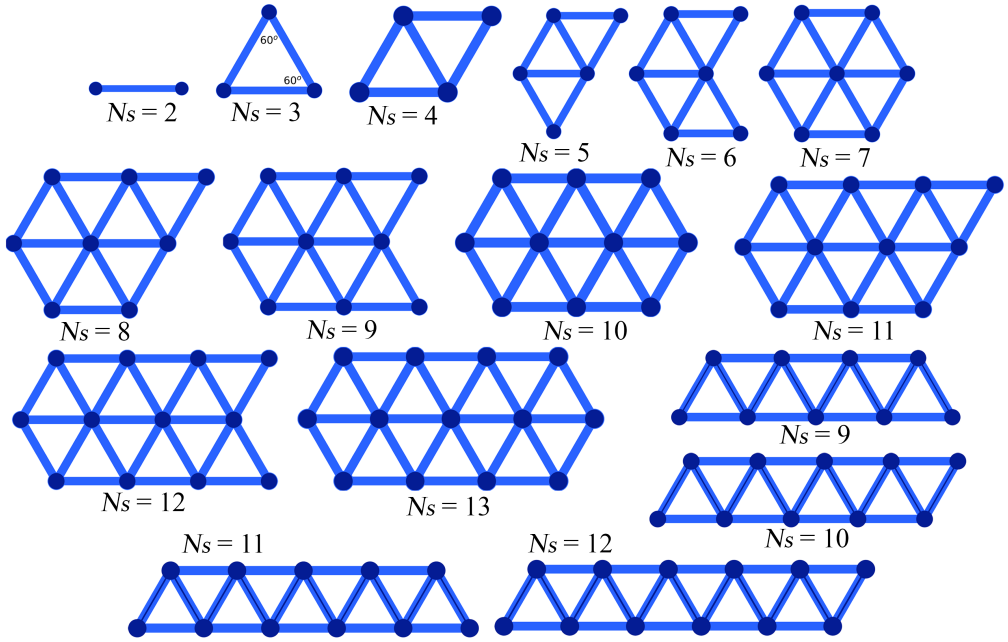

Fig. 16: Design of finite size of moiré triangular lattice arranged in single and double chain (hexagonal) configurations, with the number of sites varying from $N_s = 2, \cdots, 13$.

triangular lattices of varying sizes, ranging from the smallest with $N_s = 2$ to the largest with $N_s = 13$. Additionally, we explore different shapes, including single chains and double-chain (hexagonal) lattices. Fragments of the moiré triangular lattice are depicted in Figure 16.

As demonstrated in our analysis of a two-site, two-particle many-body problem, placing two particles on two sites results in six possible configurations and requires solving a (6×6) Hamiltonian matrix. In this study, we aim to explore all possible particle arrangements within our lattice system. However, accounting for all correlations in periodic systems is impractical due to the vast size of the Hilbert space. Therefore, we concentrate on finite-sized systems to fully capture the effects of correlations.

3 Result and Discussion

This section examines the many-body problems in a finite-size moiré triangular lattice using the Hubbard model, solved through exact diagonalization. The primary goal is to investigate the emergence of kinetic magnetism associated with Nagaoka ferromagnetism by analyzing spectral energy, phase diagrams, spin transitions, and visualizing Nagaoka polarons through spin density.

As briefly mentioned in Section 1.4.1 of the Introduction, Nagaoka ferromagnetism can be observed in a lattice system that is at half-filling with the addition of one electron or hole. The system is dominated by on-site Coulomb interaction, leading to a ground state which has high total spin.

3.1 Spectral energy analysis for total spin calculation

First, we analyze spectral energy to determine the total spin S. Figure 17 shows the spectral energy for a finite triangular lattice with number of sites $N_s = 4$, at half-filling with number of electron $N_e = N_s = 4$ particles, and the spectral energy with one electron above half-filling $N_e = N_s + 1 = 5$. The parameters used are hopping energy $t = -3.0$ meV, on-site Coulomb force $U = 1000$ meV, dielectric constant $\epsilon = 10$ (values provided by Ref. [38]), and approximate twist angle $\theta \approx 3.0^o$. The angle is considered approximate because it is not directly included as a variable in the exact diagonalization calculations. Instead, its value is derived from the relationship between the twist angle and hopping energy, as shown in the tight-binding analysis in Figure 12. By defining the twist angle, we confirm that the finite triangular lattice originates from TMDs. A large U value ensures the system experiences strong correlation effects, satisfying one of Nagaoka's conditions where $U \gg t$.

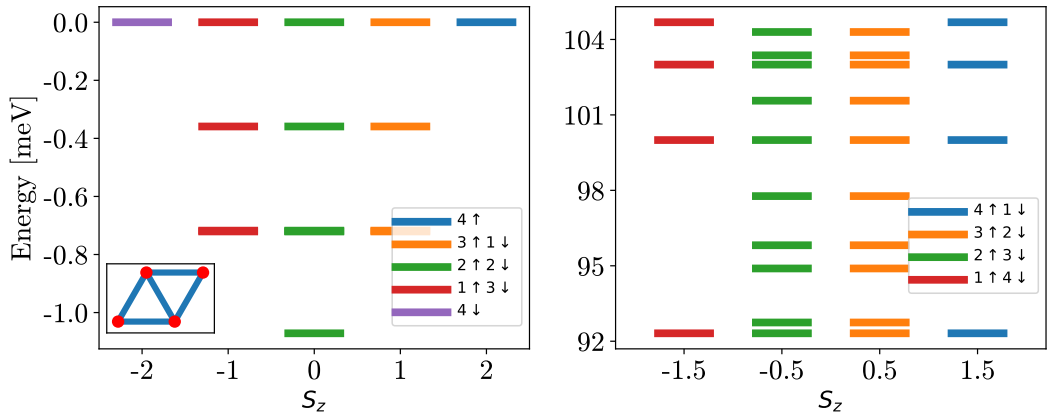

Fig. 17: Spectral energy of finite triangular lattice $N_s = 4$ sites with half-filling $N_e = N_s$ (left) and one electron above half-filling $N_e = N_s + 1$ (right). The parameter values are $t = -3.0$ meV, $U = 1000$ meV, and $\epsilon = 10$.

The spectral energy is plotted for all possible electron configuration for $N_s = 4$ at half-filling. As this system has 4 electrons, by obeying Pauli exclusion we can arrange the electron as: (1) four spin up "↑" (or spin down "↓"), (2)

three spin ↑ (↓) with one spin ↓ (↑), and (3) two spin ↑ with two spin ↓. The energy of each configuration is plotted alongside their quantum spin number S_z. Configuration with opposite spin orientation (e.g. 4 ↑ with 4 ↓) shares the same S_z and energy level. Using Eq.37, the quantum spin can be calculated, but here we focus only on the ground state energy. At half-filling the ground state corresponds to the configuration of (2 ↑ 2 ↓), yielding $S_z = \frac{1}{2}(2-2) = 0$ and the total spin $S = 0.0$.

For systems above half-filling $N_e = N_s + 1$ the electron configurations can be arranged as: (1) 4 ↑ (↓) with 1 ↓ (↑), and (2) 3 ↑ (↓) with 2 ↓ (↑). The addition of one extra electron raises the energy level due to increased on-site interactions. There are also excited states that emerge with a small energy difference from the ground state. The ground state with one electron above half-filling has a total spin $S = 1.5$, which is higher than when the triangular lattice is at half-filling. This indicates the emergence of Nagaoka ferromagnetism, characterized by a high total spin in the ground state. The total spin value indicates that, as electrons spin is $|\pm\frac{1}{2}|$, there are $\frac{1.5}{0.5} = 3$ unpaired electrons with the same spin orientation in the lattice to gain the highest total spin in the ground state. Since these unpaired electrons share the same spin orientation, the material exhibits ferromagnetic behavior.

3.2 Phase diagram for observing total spin of all possible particles on the lattices

We observe the total spin of the ground state and energy gap for all particles N_e in the lattice, as displayed in Figures 18 and 19. Energy gap is the energy difference between the ground state with the first excited state. All the moiré fragments are examined in Figure 16, but only six finite sizes ($N_s = 3, \cdots, 8$) are shown here. Consider Figure 18, as it is easy to see that for finite-site 3,4,5, the total spin is highest when one electron is added to half-filling (appointed by a green arrow). For configurations below this, the total spin is limited to either 0.0 or 0.5, depending on whether the number of particles is odd or even. For instance, in the case of 3 sites, with four electrons, the total spin is 1.0, indicating that there are two unpaired electrons. This configuration is achieved by placing two electrons with opposite spins on one site and the remaining two electrons on the other two sites, resulting in arrangements such as (3 ↑ 1 ↓) or (3 ↓ 1 ↑).

When adding another electron, $N_e = N_s + 2$ (or more), the total spin decreases from having two unpaired electrons to just one unpaired electron (continuing within the 3-site system), as the other electron pairs up. Pairs of electrons have a rigid spin orientation; if one electron spins down, the other must spin up. Consequently, these pairs are less susceptible to being influenced or polarized by the spins of unpaired electrons.

The energy gap E_g in Figure 18 and 19 are observed to be relatively small and nearly zero above half-filling. This is likely because the presence of more electrons in the energy band makes it easier for additional particles to move

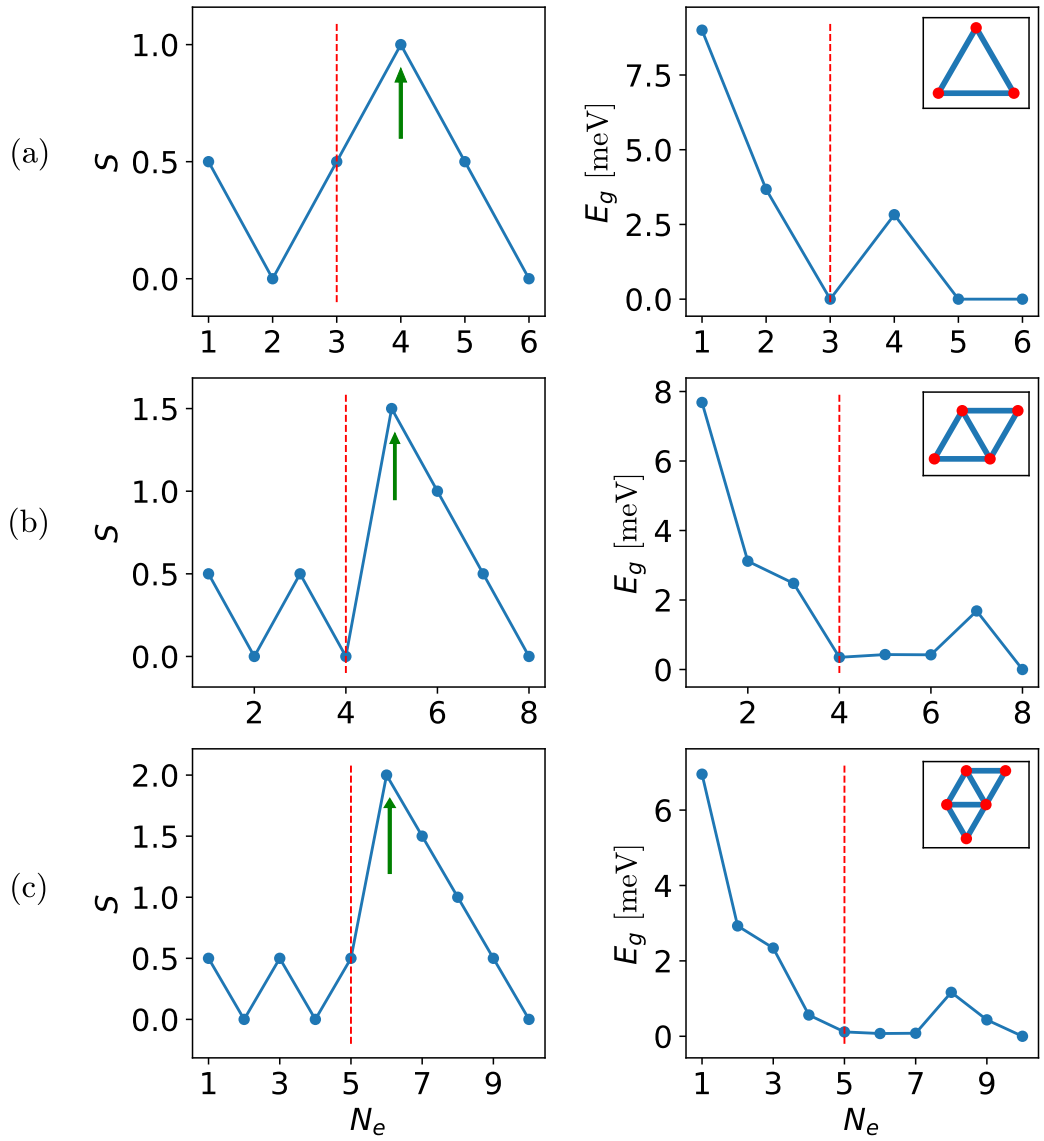

Fig. 18: (Left) total spin S of the ground state and (right) energy gap E_g between the ground state with excited states for all possible particles in the lattice. A small inset in the top-right corner of each graph illustrates the finite lattices with $N_s = 3, 4, 5$ and a green arrow denoted the highest total spin.

to the excited states, as the ground states are already populated. From this, we can infer that when the lattice has the highest total spin, the energy gap is very small. This is also already shown in Figure 17, where five electrons are placed in four sites, excited states emerge right above the ground stage with a very small energy gap in $S_z = \pm 0.5$.

Figure 19 reveals some unique observations as the finite moiré triangular lattice grows in size. In particular, hexagonal lattice 6 sites in Fig.19(a) exhibit two peaks in total spin, which is uncommon. We attribute the first peak to Nagaoka ferromagnetism in this case. Additionally, the hexagonal lattice with 7 sites and the single chain lattice with 8 sites (Fig.19(b) and (c)) show the highest total spin with the number of particles equal to N_s+3 and N_s+2, respectively.

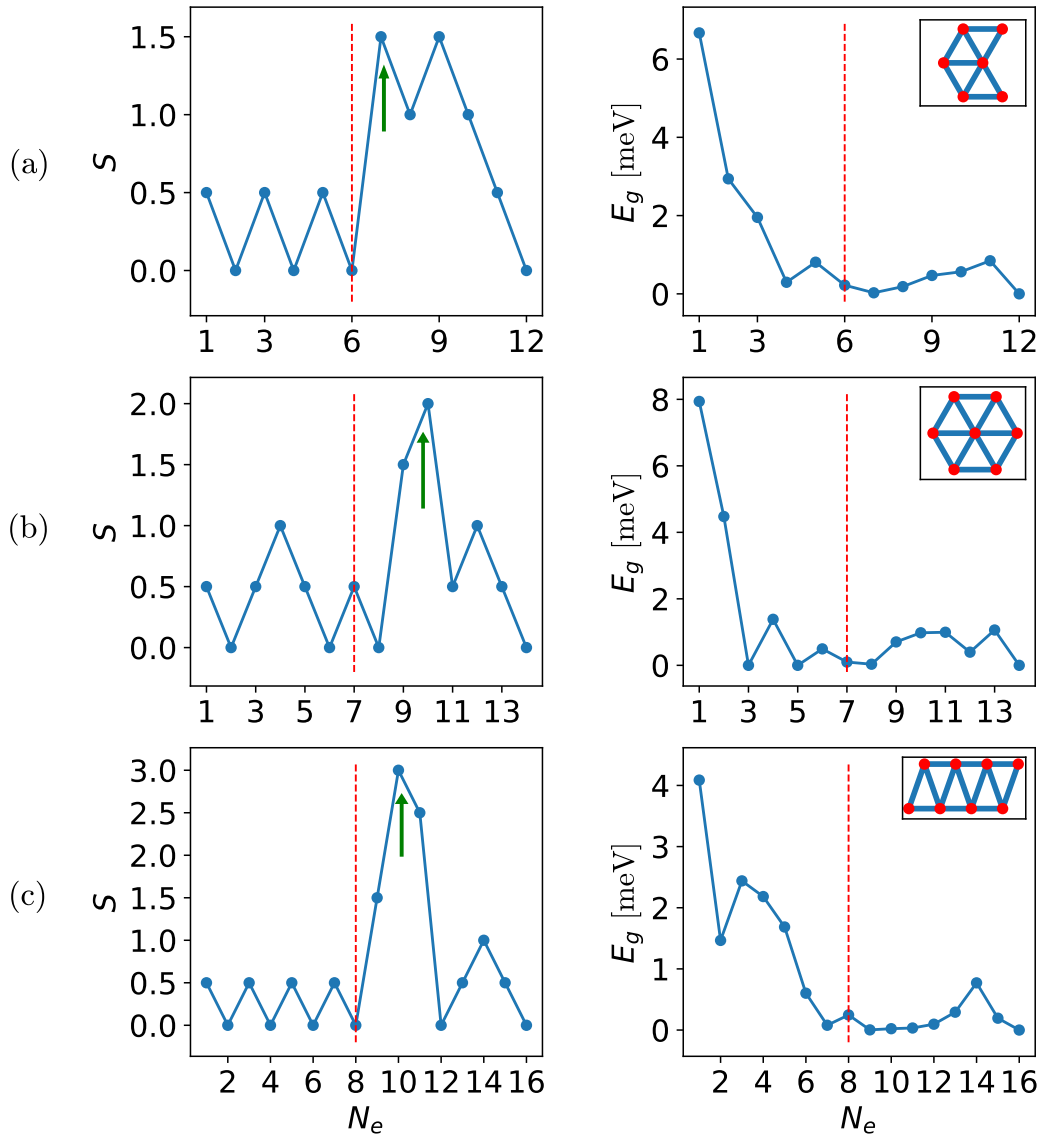

Fig. 19: (Left) total spin S of the ground state and (right) energy gap E_g between the ground state with excited states for all possible particles N_e in the lattice. A small inset in the top-right corner of each graph illustrates the finite lattices with $N_s = 6, 7, 8$ and a green arrow denoted the highest total spin.

The total spin does not immediately peak upon adding one electron $(N_s + 1)$ to the half-filling as is the case for site 3,4, and 5 in Figure 18.

Analyzing this through calculations, take site $N_s = 6$ as an example, the maximum number of particles that can occupy this site is $N_e = 12$. The highest total spin is achieved with 7 electrons, meaning there are 5 unpaired electrons (the highest number of unpaired electrons we can achieve above half-filling), giving an expected total spin $S = 5 \times \frac{1}{2} = 2.5$. In Fig.19(a), the two peaks have a total spin of 1.5, indicating that it is not the maximum total spin. A similar situation occurs in Fig.19 (b) and (c): for site 7, the maximum total spin observed is 2.0, but the calculated value should be 3.0. In site 8, the observed maximum total spin is 3.0, while the calculated value is expected to

be 3.5. This suggests that higher total spin can still be achieved in these three sites, resulting in stronger ferromagnetism.

3.3 Spin transition as the dielectric constant ϵ varies

After analyzing all finite triangular lattices from $N_s = 2$ to $N_s = 13$ in the previous section, we demonstrated the emergence of Nagaoka kinetic magnetism driven by spin arrangement and on-site interactions. Our next objective is to address questions raised by the earlier observation: why did some lattice sites not achieve the highest expected total spin, and what caused this? To begin, we recall the parameters used: $U = 1000$ meV, $t = -3$ meV, and $\epsilon = 10$. These values satisfy the Nagaoka condition of $U \gg t$, now we will explore varying the dielectric constant ϵ. Dielectric constant reflects a material's responsiveness to an electric field, with higher values indicating greater ease of polarization. We will vary ϵ from 2,4,6,...,16 to investigate whether higher total spin can be achieved at each site and to assess how stable the magnetism is with changes in dielectric constant. Adjusting the dielectric constant is more feasible experimentally, allowing for better control over the lattice.

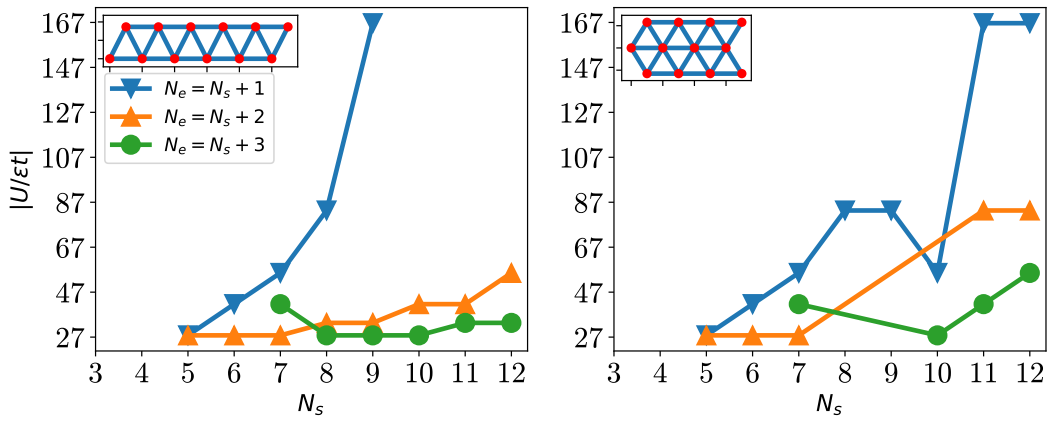

Fig. 20: The spin transition, resulting from a change in total spin caused by changes in ϵ is expressed as the ratio $|\frac{U}{\epsilon t}|$, known as interaction strength, with $U = 1000\text{meV}, t = -3.0\text{meV}$. The small figure showing the 7-site lattice, for both single-chain (left) and double-chain (right), illustrates the general structure of the triangular lattice N_s of each graph. All total spin and ϵ values are presented in Appendix A.

Figure 20 illustrates the spin transition for lattices with one, two, three particles above half-filling ($N_s + 1, N_s + 2, N_s + 3$). The spin transition refers to the change or reduction in total spin S from its maximum to minimum values as the dielectric constant ϵ varies. In the graph, we label ϵ at which the total spin starts to decrease: for example, if the total spin is maximized at $\epsilon = 4$ and decreases at $\epsilon = 6$, we mark $\epsilon = 4$. On the y-axis, we plot the ratio U to ϵt, where U and t are constants. A smaller ϵ results in a larger ratio, which in turn strengthens ferromagnetism, and vice versa. The figure contains two graphs representing lattice sites from $N_s = 3$ to $N_s = 12$ with different geometries: (left) single chain, and (right) double-chain or hexagonal configurations.

Let's begin by examining the spin transition in single-chain lattices (left figure). No transitions occur at sites 3 and 4, indicating that the total spin remains unchanged, even when the dielectrict constant is altered from 2 to 16. The maximum total spin of site 3 is $S = 1.0$ and for site 4, it is $S = 1.5$ (see Appendix A); these values represent the highest possible total spin as determined by the calculation analysis. The spin transition starts for electron $N_s + 1$ from site 5, meaning that there's a drop in total spin as we change ϵ. For lattice 8 sites, we previously observed in Figure 19 that the total spin did not reach its maximum when $\epsilon = 10$. However, we now find that its highest total spin, $S = 3.5$ occurs when $\epsilon = 4$.

The spin transition in single-chain systems increases as the size of finite lattices grows. For the $N_s + 1$ case, the interaction strength ratio grows rapidly as the number of lattice sites increases. We did not plot the spin transition for $N_s = 10$ to $N_s = 12$ due to limited ϵ values. A high ratio enables one itinerant electron above half-filling to polarize electron spins over a larger area or more sites. Since a higher ratio indicates stronger ferromagnetism, the rapid spin transition with varying dielectric constants in the $N_s + 1$ case shows that the system with one electron above half-filling is highly unstable. Even small changes in the dielectric constant can significantly affect its ferromagnetic characteristics. For particles $N_s + 2$ and $N_s + 3$, the ratio is much lower compared to $N_s + 1$, but these systems show more stable spin transitions as the number of sites increases. As ϵ increases, the spin transition changes only slightly.

In double-chain lattices, Figure 20 (right), the spin transition trend for N_{s+1} is similar to that of the single-chain, exhibiting a rapid increase in interaction strength as the number of triangular lattices grows. A notable difference appears at site 10, where the hexagonal lattice reaches its maximum total spin at a lower interaction ratio. For particles $N_s + 2$ and $N_s + 3$, no spin transition is observed around lattice sites 8 and 9, as the total spin remains unchanged despite variations in the dielectric constant. While we observe many instances of maximum total spin as ϵ is expanded from 2 to 16, in some cases, the maximum total spin is still not reached. For instance, in the hexagonal lattice with 8 sites and $N_s + 2$, the total spin remains constant at $S = 1.0$, which is not the maximum value, and for 9 sites and $N_s + 2$, the total spin stays at $S = 0.0$. Moreover, from this analysis we observe that varying the geometries of triangular lattices results in distinct characteristics.

Expanding ϵ for further analysis of single-chain sites $N_s = 9, 10, 11, 12$. We extend the analysis for single-chain systems by examining larger sites $N_s = 9, 10, 11$, and 12, and varying dielectric constant both for $\epsilon \leq 4$ and $\epsilon \geq 16$. Details for $\epsilon \leq 4$ values are provided in Appendix B, where we also examine the spin transition for hexagonal and periodic lattices. Here, we will focus on discussing the analysis for larger dielectric constant values $\epsilon \geq 16$.

In Figure 21, we extend the analysis to larger values of ϵ, focusing specifically on single-chain sites 9 to 12. We plot the maximum total spin in the ground

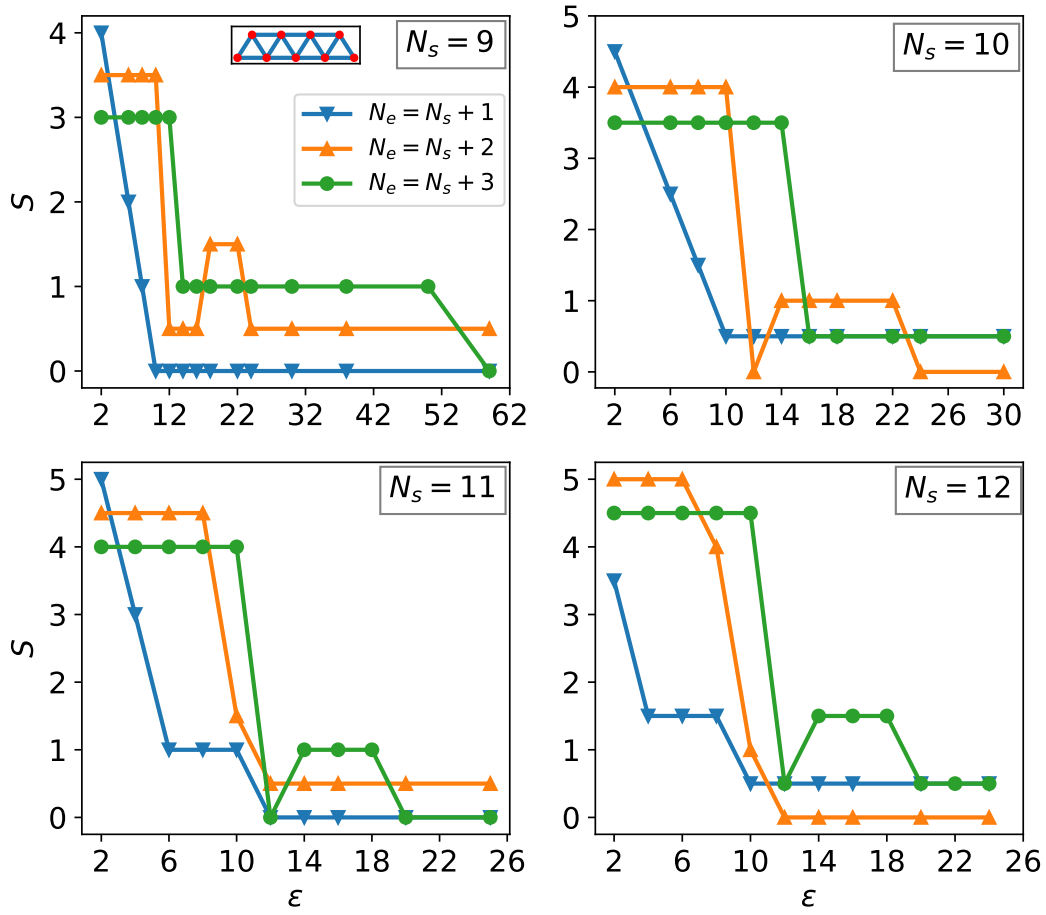

Fig. 21: The spin transition of a single-chain lattice site $N_s = 9, 10, 11, 12$ with $U = 1000$ meV, $t = -3$ meV. The dielectric constant ϵ is extended until the total spin S reaches its minimum value.

state, starting from $\epsilon = 2$, and continue until the total spin drops to its lowest value ($S = 0$ for even particles and $S = 0.5$ for odd particles).

The highest total spin occurs when ϵ is low, and it diminishes as ϵ increases. With smaller dielectric constant, the interaction strength ratio $|\frac{U}{\epsilon t}|$ becomes larger, making it easier to observe Nagaoka ferromagnetism in systems with low ϵ. This graph helps determine the optimal parameters for detecting ferromagnetic characteristics. Next for number of particle $N_s + 1$, the total spin gradually decreases as ϵ rises. Interestingly, the spin reduction in the cases of $N_s + 2$ and $N_s + 3$ is quite similar and there is unique behavior observed. For example, at site 9 with 11 particles, the total spin drops to its lowest value of $S = 0.5$ when ϵ is below 20, but then increases to $S = 1.5$ before disappearing again near $\epsilon = 24$. This reappearance of spin transition is also seen in 10-site 12 particles, 11-site 14 particles, and 12-site 15 particles systems.

Spin transition for varying geometries: single-chain and double-chain.

In this sub part we compare the total spin of the ground state between single-chain and double-chain or hexagonal finite triangular lattice. We plot the total

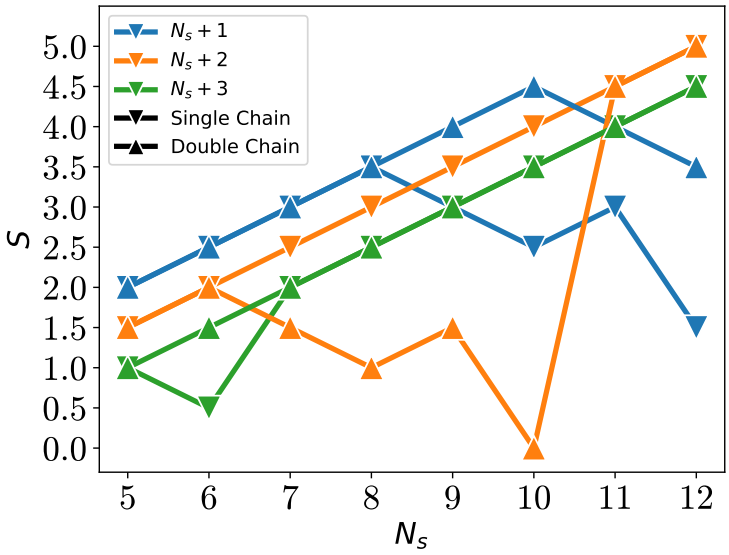

Fig. 22: The ground state total spin (S) of a single-chain and double-chain lattices with number of site from $N_s = 5$ to $N_s = 12$ and number of particle $N_e = N_s + 1, N_s + 2, N_s + 3$. Parameters: $U = 1000$ meV, $t = -3$ meV, and $\epsilon = 4.0$.

spin in Figure 22 for the number of lattice sites $N_s = 5$ to $N_s = 12$. We omit the cases for $N_s = 3, 4$ because the lattice shapes for both single-chain and double-chain configurations are identical at these sizes. All other parameters remain constant: $U = 1000$ meV, $t = -3$ meV, $\epsilon = 4$, leaving the lattice geometry as the sole differing factor. We selected $\epsilon = 4$ because, at this dielectric constant, the ground state of most finite triangular lattices achieves its maximum total spin.

For single-chain systems with $N_s + 1$ electrons, the total spin reaches its maximum up to site $N_s = 10$, but then decreases for $N_s = 11, 12$.This suggests that the 11-site and 12-site systems require a smaller dielectric constant to achieve their maximum total spin. In the double-chain case with $N_s + 1$ electrons, a smaller ϵ is needed starting at $N_s = 9$ to to reach the highest total spin. A big drop in total spin occurs for $N_s + 2$ double-chain systems between site-7 to site-10. Meanwhile, lattices with $N_s + 3$ remain mostly stable for both single-chain and double-chain configurations. From here we can see that single-chain triangular lattices are more stable, while double-chain or hexagonal lattices are less stable, particularly for $N_s + 2$ particles.

3.4 Visualization of Nagaoka polaron with spin density

In this section, we present visualizations of the spin and charge densities of electrons on the lattices. Spin density is defined as the difference between the probabilities of spin-up ($\uparrow$) and spin-down ($\downarrow$) at the same lattice site. Charge density is obtained by summing the probabilities of spin-up and spin-down electrons at the same lattice site. Charge density offers insights into the electronic properties of the system, while spin density reveals its magnetic characteristics.

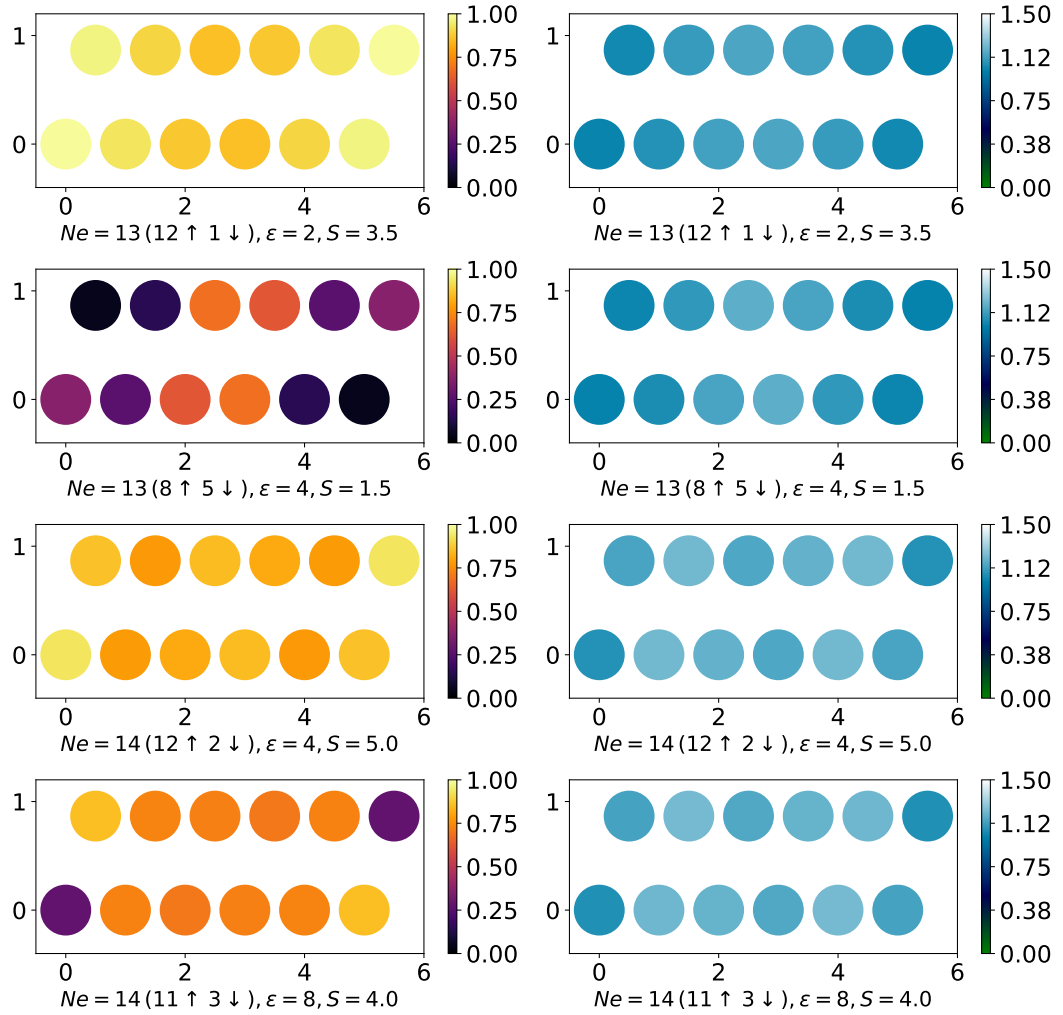

Fig. 23: Visualization of spin density (left) and charge density (right) of single-chain lattice $N_s = 12$ sites with $N_s + 1$ and $N_s + 2$ electrons. Parameter values: $t = -3$ meV, $U = 1000$ meV.

Spin and charge density of 12-site single-chain lattice.
Figure 23 illustrates the spin and charge densities for site $N_s = 12$ of a single-chain triangular lattice with $N_e = N_s+1 = 13$ and $N_e = N_s+2 = 14$ electrons, each system having two different dielectric constant values, ϵ. From the charge density analysis (right-graph), we observe that electron charge is distributed across the lattice sites with slight variations between them, and the lowest density tends to concentrate at the edges of the lattices.

While the charge is evenly distributed for 12 and 13 electrons, the spin density reveals a different pattern. Focusing on the top-left graph, which shows a 12-site single-chain with 13 electrons, arranged with 12 spin-up and 1 spin-down, and a value of $\epsilon = 2$, we obtain a maximum total spin $S = 3.5$. The maximum total spin is lower than expected for this configuration, which is due to parameter ϵ. The darker color in the center of the chain indicates a smaller difference between spin-up and spin-down, suggesting that the probabilities of this two spins are nearly equal in this region. This indicates that the probabil-

ity of a spin-down electron (from $12 \uparrow 1 \downarrow$ configuration) is spread across the middle of the chain. Meanwhile, the higher spin density at the edges indicates a greater likelihood of unpaired electrons, which in this case are spin-up. This observation of spin density reveals the presence of a Nagaoka bubble or Nagaoka polaron, similar to what is described in Ref. [7]. One itinerant electron remains in the center, polarizing the surrounding spins. However, we cannot observe the full extent of the bubble as shown in Figure 5 due to the limited size of our lattice system, which consists of only 12 sites.

Next, we use a different configuration ($8 \uparrow 5 \downarrow$), which results in a lower maximum total ground state spin of $S = 1.5$ when $\epsilon = 4$. In this case, the spin density is concentrated in the center, while paired electrons tend to remain at the corners. This demonstrates that altering the electron configuration within the same system leads to significant changes in the system's ferromagnetic behavior.

Further analysis, we add one more electron to the system, resulting in a 12-site single-chain triangular lattice with 14 electrons. By applying $\epsilon = 4$ and arranging the electron configuration ($12 \uparrow 2 \downarrow$), we achieve the maximum total spin of $S = 4.0$. As seen in the first spin density graph (top-left), the two spin-down electrons are spread across the central region, with a high concentration in lattice columns 1 and 4 along the x-axis. As we change the configuration into ($11 \uparrow 3 \downarrow$, as shown in the bottom-left graph), the two most concentrated paired electrons are located in the corners. From this, we observe that the spin-down electrons, being fewer in number, have more freedom and tend to stay farther apart from each other.

Spin and charge density of 12-site hexagonal lattice.
We examine the spin and charge densities of a 12-site system arranged in a hexagonal or double-chain structure, as shown in Figure 24. In this study, we add one, two, and three spin-down electrons to the system while maintaining a dielectric constant of $\epsilon = 2$. The charge density is evenly distributed for 13 particles($12 \uparrow 1 \downarrow$), and for 14 particles ($12 \uparrow 2 \downarrow$), we observe a higher probability concentrated on two sites in the middle. For 15 particles ($12 \uparrow 3 \downarrow$), the charge density forms a unique pattern, with a denser charge concentrated around a less dense site located at column 2 along the x-axis.

In all three cases, where the system reaches maximum total spin, the spin density is fairly evenly distributed across each lattice, in contrast to the single-chain configurations. In the case of one electron above half-filling, the spin-down electron pairs with the spin in the central region. For configurations with two and three spin-down electrons, the denser distribution of paired electrons follows the charge density pattern. From this, we observe that adding more spin-down electrons beyond half-filling decreases the spin density at each site. This is because the additional electrons reduce the probability of unpaired electrons at the sites, leading to weaker ferromagnetic effects. Therefore, it is challenging to determine the extent to which a single itinerant electron influences its surroundings or to observe the Nagaoka bubble, as depicted in

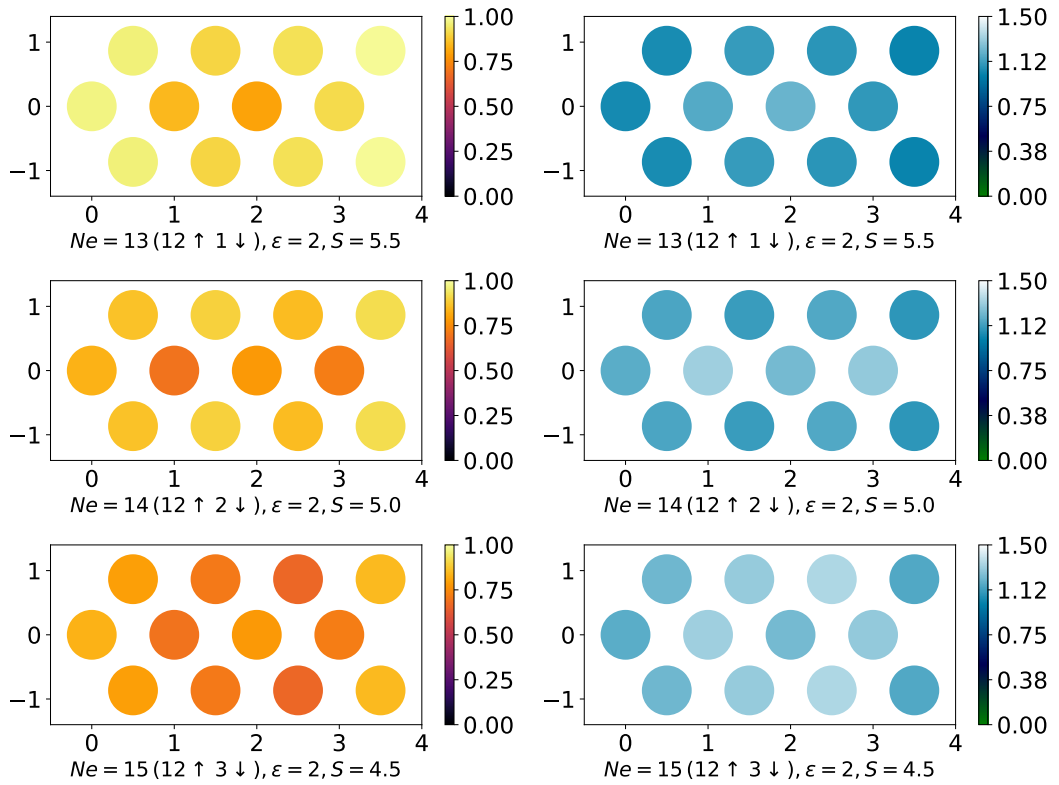

Fig. 24: Visualization of spin density (left) and charge density (right) of double-chain lattice $N_s = 12$ sites with $N_s + 1$, $N_s + 2$, and $N_s + 3$ electrons. Parameter values: $t = -3$ meV, $U = 1000$ meV.

Figure 5, due to the small size of our finite triangular lattice system. For further observation, additional spin and charge density results are provided in Appendix C.

4 Conclusion

Nagaoka ferromagnetism occurs when a half-filled system gains an additional electron or hole. By ensuring that the system maintains a strong on-site Coulomb interaction compared to the hopping energy, the ground state achieves maximum total spin [30]. In this work, we focus on finite-size triangular lattices of twisted TMDs, limited to a number of sites from $N_s = 2$ to $N_s = 13$, examining two geometries: single-chain and double-chain. We observe the emergence of Nagaoka ferromagnetism in these finite lattices by adding a single electron to the half-filling ($N_s + 1$), resulting in a ground state with maximum total spin. Larger lattices exhibit higher maximum total spin, leading to stronger ferromagnetic behavior. Additionally, at some finite systems, the maximum total spin appear when adding two or three electrons ($N_s + 2$ and $N_s + 3$), indicating that Nagaoka ferromagnetism remains present with two and three electrons above half-filling.

We note that varying geometries result in distinct magnetic properties, and our analysis shows that the single-chain configuration is more stable as the number of sites increases, compared to the double-chain. We further explore this by modifying the dielectric constant which related to the interaction strength factor, as it is feasible to adjust in experimental setups. The triangular lattices with $N_s + 2$ and $N_s + 3$ electrons exhibit more stable ferromagnetic properties as the dielectric constant varies. This indicates that the total spin of the lattice either remains constant or changes only slightly with adjustments in the dielectric constant, eliminating the need to rely on specific dielectric values to achieve ferromagnetism. In contrast, for finite triangular lattices with $N_s + 1$ electrons, we observe significant instability, with the total spin decreasing rapidly as the dielectric constant increases.

As this study focuses on small segments of twisted triangular lattices of TMDs, Nagaoka ferromagnetism can still be observed in larger systems. Moreover, the tunability of TMDs through the twisting angle opens up the possibility of constructing triangular lattices that exhibit Nagaoka ferromagnetism based on the parameters established in this work.

References

[1] R. Bistritzer and A. H. MacDonald, "Moiré bands in twisted double-layer graphene," *Proceedings of the National Academy of Sciences*, vol. 108, no. 30, pp. 12233–12237, 2011.

[2] S. Manzeli, D. Ovchinnikov, D. Pasquier, O. Yazyev, and A. Kis, "2d transition metal dichalcogenides," *Nature Reviews Materials*, vol. 2, p. 17033, 2017.

[3] D. Xiao, G.-B. Liu, W. Feng, X. Xu, and W. Yao, "Coupled spin and valley physics in monolayers of mos_2 and other group-vi dichalcogenides," *Physical Review Letters*, vol. 108, p. 196802, 2012.

[4] F. Wu, T. Lovorn, E. Tutuc, and A. MacDonald, "Hubbard model physics in transition metal dichalcogenide moiré bands," *Phys. Rev. Lett.*, vol. 121, p. 026402, Jul 2018.

[5] N. R. Wilson, P. V. Nguyen, K. Seyler, P. Rivera, A. J. Marsden, Z. P. Laker, G. C. Constantinescu, V. Kandyba, A. Barinov, N. D. Hine, X. Xu, and D. H. Cobden, "Determination of band offsets, hybridization, and exciton binding in 2d semiconductor heterostructures," *Science Advances*, vol. 3, no. 2, p. e1601832, 2017.

[6] N. Ashcroft and N. Mermin, *Solid State Physics*. New York: Holt, Rinehart and Winston, 1976.

[7] M. Lebrat, M. Xu, L. Kendrick, A. Kale, Y. Gang, P. Seetharaman, I. Morera, E. Khatami, E. Demler, and M. Greiner, "Observation of nagaoka polarons in a fermi–hubbard quantum simulator," *Nature*, vol. 629, pp. 317–322, 2024.

[8] D. M. Kennes, M. Claassen, L. Xian, A. Georges, A. Millis, J. Hone, C. Dean, D. N. Basov, A. Pasupathy, and A. Rubio, "Moiré heterostructures as a condensed-matter quantum simulator," *Nature Physics*, vol. 17, no. 2, pp. 155–163, 2021.

[9] Y. Liao, W. Cao, J. Connell, Z. Chen, and Y. Lin, "Evolution of moiré profiles from van der waals superstructures of boron nitride nanosheets," *Scientific Reports*, vol. 6, p. 26084, 2016.

[10] Y. Jiang, X. Lai, K. Watanabe, T. Taniguchi, K. Haule, J. Mao, and E. Y. Andrei, "Charge order and broken rotational symmetry in magic-angle twisted bilayer graphene," *Nature*, vol. 573, pp. 91–95, 2019.

[11] A. Geim and I. Grigorieva, "Van der waals heterostructures," *Nature*, vol. 499, pp. 419–425, 2013.

[12] K. Kim, A. DaSilva, S. Huang, B. Fallahazad, S. Larentis, T. Taniguchi, K. Watanabe, B. LeRoy, A. MacDonald, and E.Tutuc, "Tunable moiré bands and strong correlations in small-twist-angle bilayer graphene," *Pro-*

ceedings of the National Academy of Sciences of the United States of America, vol. 114, pp. 3364–3369, March 2017.

[13] Y. Cao, V. Fatemi, A. Demir, S. Fang, S. Tomarken, J. Luo, J. Sanchez-Yamagishi, K. Watanabe, T. Taniguchi, E. Kaxiras, R. Ashoori, and P. Jarillo-Herrero, "Correlated insulator behaviour at half-filling in magic-angle graphene superlattices," *Nature*, 2018.

[14] Y. Tang, L. Li, T. Li, Y. Xu, S. Liu, K. Barmak, K. Watanabe, T. Taniguchi, A. MacDonald, J. Shan, and K. Mak, "Simulation of hubbard model physics in wse2/ws2 moiré superlattices," *Nature*, vol. 579, pp. 353–358, 2020.

[15] E. Regan, D. Wang, C. Jin, M. Utama, B. Gao, X. Wei, S. Zhao, W. Zhao, Z. Zhang, K. Yumigeta, M. Blei, J. Carlström, K. Watanabe, T. Taniguchi, S. Tongay, M. Crommie, A. Zettl, and F. Wang, "Mott and generalized wigner crystal states in wse2/ws2 moiré superlattices," *Nature*, vol. 579, pp. 359–363, 2020.

[16] L. Wang, E.-M. Shih, A. Ghiotto, L. Xian, D. Rhodes, C. Tan, M. Claassen, D. Kennes, Y. Bai, B. Kim, K. Watanabe, T. Taniguchi, X. Zhu, J. Hone, A. Rubio, A. Pasupathy, and C. Dean, "Correlated electronic phases in twisted bilayer transition metal dichalcogenides," *Nature Materials*, vol. 19, pp. 861–866, 2020.

[17] Y. Cao, V. Fatemi, S. Fang, A. Sharpe, K. Watanabe, T. Taniguchi, E. Kaxiras, C. Dean, and P. Kim, "Unconventional superconductivity in magic-angle graphene superlattices," *Nature*, vol. 556, pp. 43–50, 2018.

[18] Y. Zhang, N. Yuan, and L. Fu, "Moiré quantum chemistry: Charge transfer in transition metal dichalcogenide superlattices," *Phys. Rev. B*, vol. 102, p. 201115, 2020.

[19] A. Splendiani, L. Sun, Y. Zhang, T. Li, J. Kim, C. Chim, G. Galli, and F. Wang, "Emerging photoluminescence in monolayer mos2," *Nano letters*, vol. 10, no. 4, pp. 1271–1275, 2010.

[20] K. Mak, C. Lee, J. Hone, J. Shan, and T. Heinz, "Atomically thin mos2: A new direct-gap semiconductor," *Phys. Rev. Lett.*, vol. 105, p. 136805, Sep 2010.

[21] Z. Zhu, Y. Cheng, and U. Schwingenschlögl, "Giant spin-orbit-induced spin splitting in two-dimensional transition-metal dichalcogenide semiconductors," *Phys. Rev. B*, vol. 84, p. 153402, Oct 2011.

[22] C. Zhang, C.-P. Chuu, X. Ren, M.-Y. Li, L.-J. Li, C. Jin, M.-Y. Chou, and C.-K. Shih, "Interlayer couplings, moiré patterns, and 2d electronic superlattices in twisted bilayer transition metal dichalcogenides," *Science Advances*, vol. 3, no. 9, p. e1601459, 2017.

[23] T. Devakul, V. Crépel, Y. Zhang, and L. Fu, "Magic in twisted transition metal dichalcogenide bilayers," *Nature communications*, vol. 12, p. 6730, November 2021.

[24] A. Carvalho, P. Trevisanutto, S. Taioli, and A. Castro Neto, "Computational methods for 2d materials modelling," *Reports on Progress in Physics*, vol. 84, p. 106501, 2021.

[25] J. Hubbard, "Electron correlations in narrow energy bands," *Proceedings of the Royal Society of London. Series A. Mathematical and Physical Sciences*, vol. 276, no. 1365, pp. 238–257, 1963.

[26] M. Gibertini, M. Koperski, A. F. Morpurgo, *et al.*, "Magnetic 2d materials and heterostructures," *Nature Nanotechnology*, vol. 14, pp. 408–419, 2019.

[27] K. F. Mak, J. Shan, and D. C. Ralph, "Probing and controlling magnetic states in 2d layered magnetic materials," *Nature Reviews Physics*, vol. 1, pp. 646–661, 2019.

[28] B. Huang, M. A. McGuire, A. F. May, *et al.*, "Emergent phenomena and proximity effects in two-dimensional magnets and heterostructures," *Nature Materials*, vol. 19, pp. 1276–1289, 2020.

[29] T. Song, Q.-C. Sun, E. Anderson, C. Wang, J. Qian, T. Taniguchi, K. Watanabe, M. A. McGuire, R. Stöhr, D. Xiao, T. Cao, J. Wrachtrup, and X. Xu, "Direct visualization of magnetic domains and moiré magnetism in twisted 2d magnets," *Science*, vol. 374, no. 6571, pp. 1140–1144, 2021.

[30] Y. Nagaoka, "Ferromagnetism in a narrow, almost half-filled s-band," *Physical Review*, vol. 147, no. 1, pp. 392–405, 1966.

[31] J. P. Dehollain, U. Mukhopadhyay, V. P. Michal, Y. Wang, S. Wagner, C. Reichl, W. Wegscheider, M. S. Rudner, E. Demler, F. Kuemmeth, and J. R. Petta, "Nagaoka ferromagnetism observed in a quantum dot plaquette," *Nature*, vol. 579, pp. 528–533, 2020.

[32] T. Thakur and B. Szafran, "Nagaoka ferromagnetism in an array of phosphorene quantum dots," *Scientific Reports*, vol. 13, p. 18796, 2023.

[33] J. M. B. Lopes dos Santos, N. M. R. Peres, and A. H. Castro Neto, "Graphene bilayer with a twist: Electronic structure," *Phys. Rev. Lett.*, vol. 99, p. 256802, Dec 2007.

[34] A. Güçlü, P. Potasz, M. Korkusinski, and P. Hawrylak, *Graphene Quantum Dots*. Berlin Heidelberg: Springer, 2014.

[35] W. Lima, F. Araújo, D. Da Costa, S. Sena, and J. Pereira, "Tight-binding model in first and second quantization for band structure calculations," *Brazilian Journal of Physics*, vol. 52, 04 2022.

[36] H. Fehske, R. Schneider, and A. Weiße, eds., *Computational Many-Particle Physics*, vol. 739 of *Lecture Notes in Physics*. Springer, 2008.

[37] N. Morales-Durán, N. Hu, P. Potasz, and A. MacDonald, "Nonlocal interactions in moiré hubbard systems," *arXiv preprint arXiv:2108.03313v2*, 2021. Published in Phys. Rev. Lett., 128, 217202 (2022).

[38] W. Pasek, M. Kupczynski, and P. Potasz, "Magnetic properties of moiré quantum dot arrays," *arXiv preprint arXiv:2208.04636v4*, 2023. Published in Phys. Rev. B, 108, 165152 (2023).

A Maximum total spin of all finite-site triangular lattices

We provide graphs displaying the maximum total spin S of the ground state for each finite-size triangular lattice in both single-chain and double-chain (hexagonal) configurations and the dielectrict constant ϵ correspond to it. This observation is based on varying ϵ values from 2,4,...,16, with an on-site interaction of $U = 1000$ meV, hopping energy $t = -3$ meV, and the approximate twisted angle $\theta \approx 3.0^o$. The data from the table is also visualized as interaction strength ratio in Figure 20, found in Section 3.3.

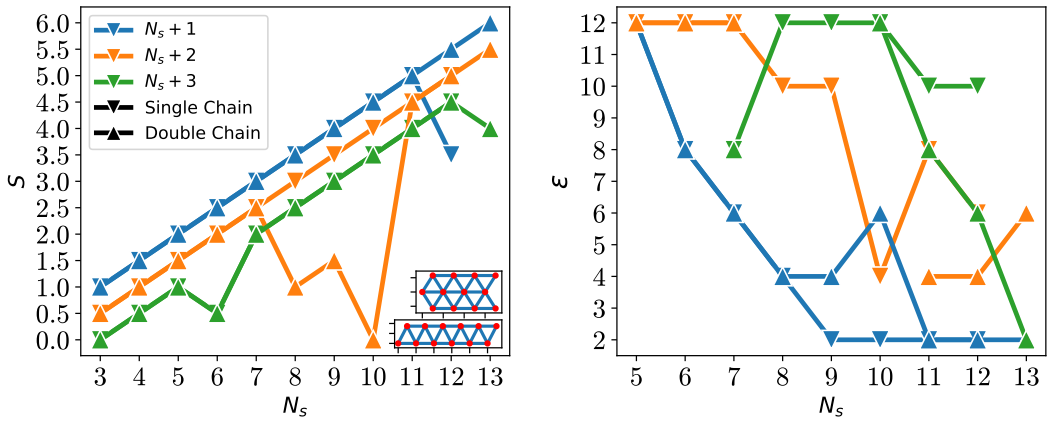

Fig. 25: Maximum total spin values for single-chain and hexagonal lattices with variation $\epsilon = 2, 4, \cdots, 16$. Parameter: $U = 1000$ meV, $t = -3$ meV.

The ϵ value indicates when the system maintains the highest total spin before it begins to decrease as ϵ increases. In some cases on the Figure 25 (right), the ϵ value is not provided because the total spin remains unchanged within that permittivity range, such as for 3-site and 4-site lattices. In other cases, we did not observe the highest total spin, such as in the 12-site single-chain system with $N_s + 1 = 13$ particles and a big drop for double-chain systems with $N_s + 2$ particles. Therefore, in Appendix B, we extended the analysis to ϵ values smaller than 2 to determine if the maximum total spin can be achieved there especially for the 12-site single-chain system.

B Further analysis of spin transition

In this section we present graphs of spin transitions for various cases, including extended ϵ values, hexagonal lattices, and periodic lattices.

Examine the spin transition of single-chain lattices for $\epsilon \leq 4$.

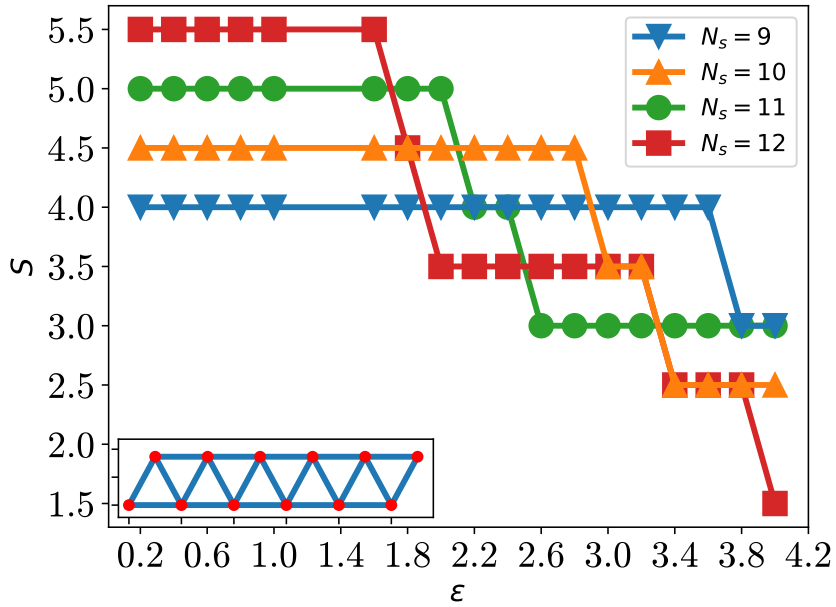

Fig. 26: Spin transition of single-chain triangular lattice for $N_s = 9, 10, 11, 12$ with $\epsilon \leq 4$ for $N_e = N_s + 1$. Parameter: $U = 1000$ meV, $t = -3$ meV.

Figure 26 displays the total spin (S) of a single-chain with $N_s = 9$ to $N_s = 12$ sites for $N_s + 1$ particles, observing dielectric constant from $\epsilon = 0.2$ to $\epsilon = 4.0$. From this graph, we can see that larger chains reach their maximum total spin at lower ϵ values. We can also see the maximum total spin $S = 5.5$ of $N_s = 12$ is achieved at $\epsilon = 1.6$, which explains why its maximum is not visible in Figure 21.

Analysis the spin transition of double-chain triangular lattices for site $N_s = 8, 9$.

In Figure 21, no spin transition was observed in the double-chain lattice at sites 8-9 for $N_s + 2$ and $N_s + 3$ particles within the range $\epsilon = 2, 4, 6, \cdots, 16$. Therefore, in Figure 27, we extended the permittivity range to capture the lowest total spin. For the hexagonal 8-site lattice with 9 particles, the total spin remains constant at $S = 1.0$ and only begins to decrease when $\epsilon > 50$. With 10 particles, the total spin stays at $S = 2.5$ and drops after $\epsilon = 20$. Similarly, for the hexagonal 9-site lattice, the total spin for 11 and 12 particles decreases when $\epsilon = 20$. In both cases, we do not observe the highest total spin for $N_s + 2$. From the small epsilon analysis in Figure 26, it is clear that the highest total spin for $N_s + 2$ occurs when $\epsilon < 2$. Moreover, for both site numbers, the behavior of Ns+1 particles is similar, showing a rapid drop in

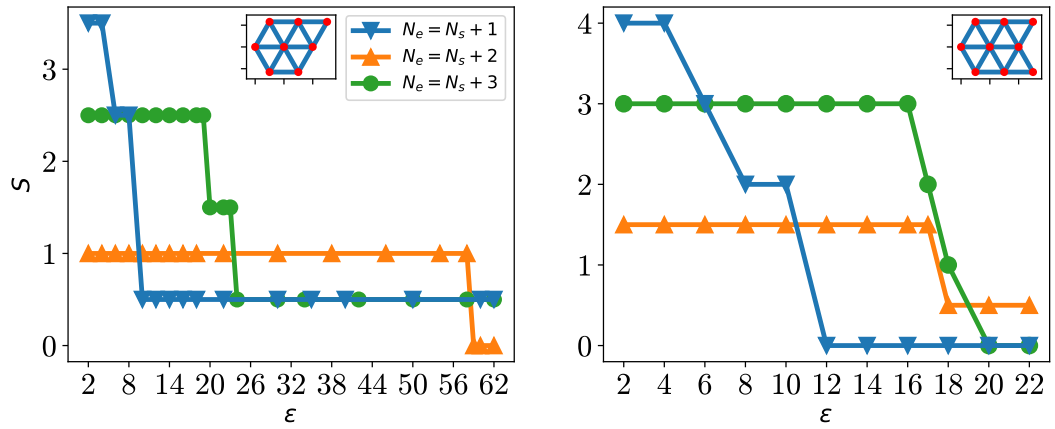

Fig. 27: Extended ϵ observations for spin transitions in double-chain lattices with $N_s = 8$ (left) and $N_s = 9$ sites (right). The ϵ values are extended until the lowest spin is reached for $N_s + 1, N_s + 2$, and $N_s + 3$ particles. Parameter: $U = 1000$ meV, $t = -3$ meV.

total spin.

The spin transition of double-chain triangular lattices.
Spin transition for double-chain or hexagonal lattices with $N_s = 10, 11, 12, 13$

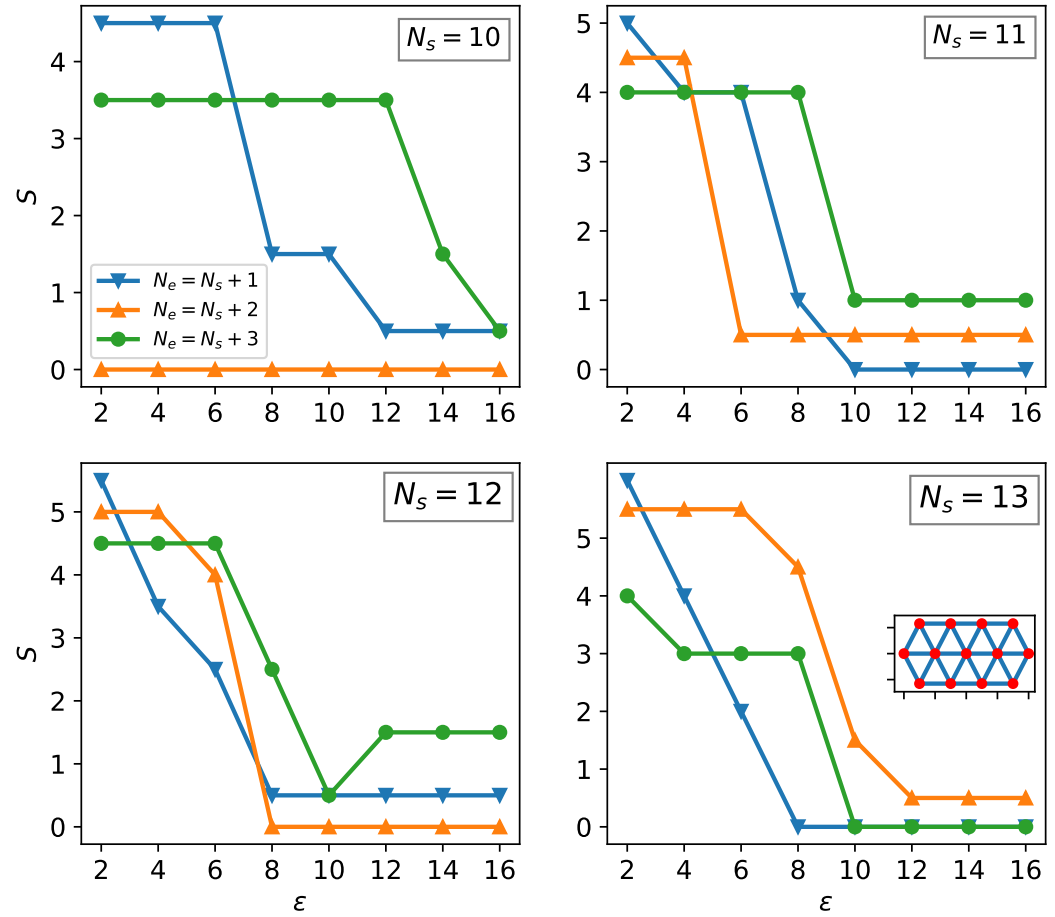

Fig. 28: The spin transition of double-chain or hexagonal lattices site $N_s = 10, 11, 12, 13$ with $U = 1000$ meV, $t = -3$ meV. The dielectric constant range is $\epsilon = 2, 4, 6, \cdots, 16$.

sites are shown in Figure 28. The parameter range is $\epsilon = 2, 4, 6, \cdots, 16$ with $U = 1000$ meV and hopping energy $t = -3$ meV. For the hexagonal 10-site lattice with 12 particles, no spin transition is observed, and the total spin remains at $S = 0.0$, which is the lowest possible spin, indicating the absence of any magnetic characteristics. For triangular lattice $N_s = 11, 12, 13$, the spin transition of $N_s + 1, N_s + 2$, and $N_s + 3$ particles exhibit a similar decline compared to site-10.

The spin transition of periodic single-chain and periodic hexagonal triangular lattices.

In this case, we introduce periodic lattices for both single-chain and double-chain systems. The periodicity is defined along the x-direction by linking the left and right edges of the triangular lattice. We can create periodic lattices for single-chain systems with 10 and 12 sites, but not for 11 sites, due to the periodic lattice requirement, which involves connecting the left and right edges (similar to fitting a key into a keyhole). The same applies to constructing periodic double-chain lattices. This periodicity is represented by adding nearest-neighbor connections when constructing the Hamiltonian.

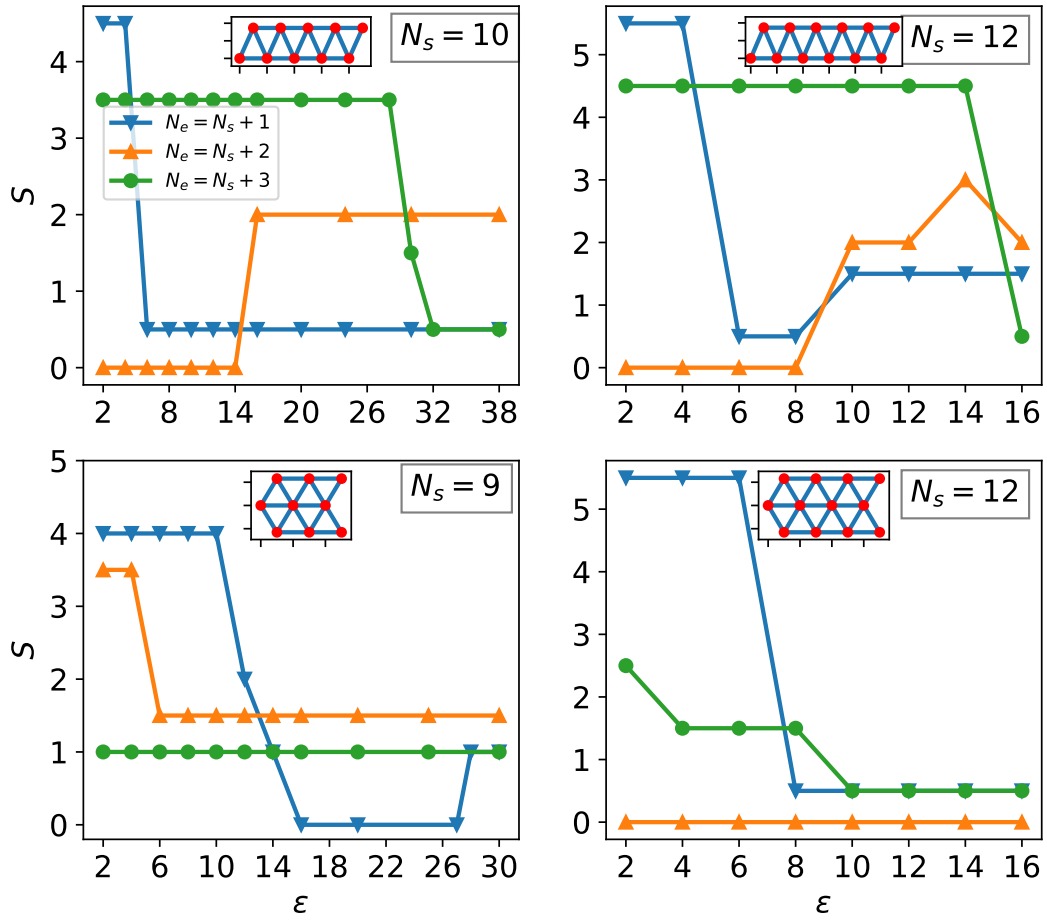

Fig. 29: The spin transition of periodic double-chain or hexagonal lattices site $N_s = 10, 11, 12, 13$ with $U = 1000$ meV, $t = -3$ meV. The dielectric constant range is $\epsilon = 2, 4, 6, \cdots$.

Figure 29 shows the spin transition for our periodic lattices: $N_s = 10, 12$ for single-chain and $N_s = 9, 12$ for double-chain. The parameter values are $U = 1000$ meV and $t = -3$ meV, with ϵ depending on the lattices. The spin drops sharply for periodic single-chains with $N_s + 1$ at both sites, while it remains more stable with $N_s + 3$. A distinct trend is observed for $N_s + 2$: at low dielectric constant values, the total spin is minimal, indicating an absence of magnetic characteristics, but as the dielectric constant increases, the total spin rises. In the case of periodic double-chain systems, no spin transition is observed at site-9 with $N_s + 3$ and site-12 with $N_s + 2$.

C Charge and spin density of periodic triangular lattices

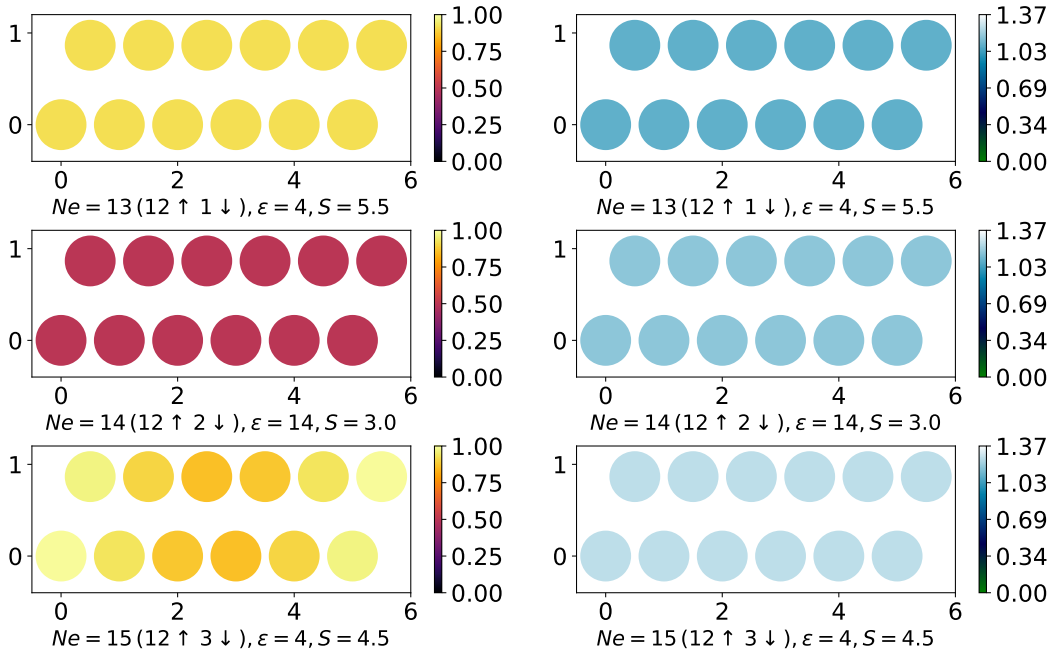

Fig. 30: Visualization of spin density (left) and charge density (right) of periodic single-chain lattice $N_s = 12$ sites with $N_s + 1$, $N_s + 2$, and $N_s + 3$ electrons. Parameter values: $t = -3$ meV, $U = 1000$ meV.

This section illustrates the spin density and charge density for a periodic triangular lattice with 12 sites, focusing on both single-chain and double-chain configurations. We present the spin and charge density of a periodic single-chain with N_s+1 and N_s+3 particles in Figure 30, with their maximum total spin. In contrast, N_s+2 does not achieve its maximum total spin, as noted in Appendix B Figure 29, resulting in a darker appearance of the spin density.

We present the spin and charge density for a periodic double-chain with 12 sites and particles N_s+1 and N_s+3 in Figure 31. The total spin of the ground state for $N_s + 2$ remains at its minimum, indicating that Nagaoka ferromagnetism is not observed in this case.

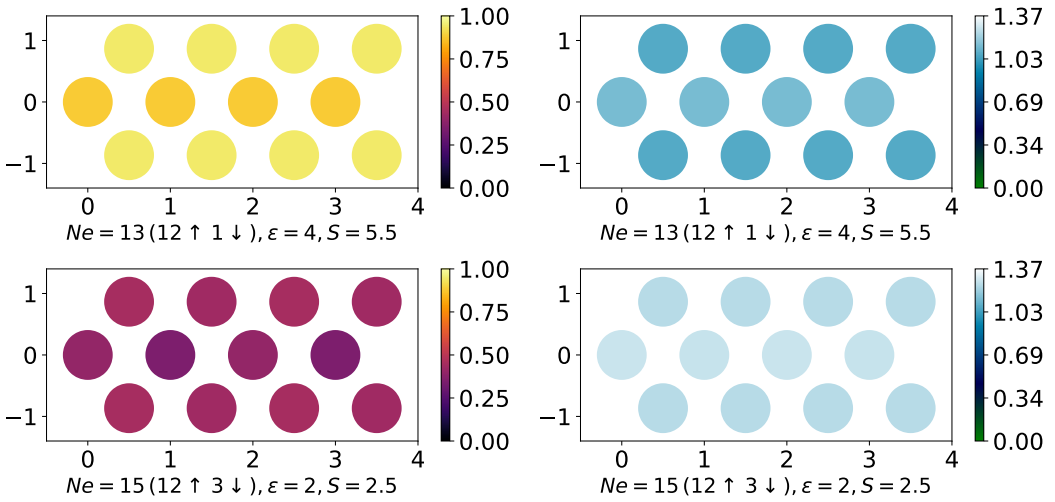

Fig. 31: Visualization of spin density (left) and charge density (right) of periodic double-chain lattice $N_s = 12$ sites with $N_s + 1$ and $N_s + 3$ electrons. Parameter values: $t = -3$ meV, $U = 1000$ meV.